Astronomy & Astrophysics manuscript no. xmmwr40 September 22, 2004
(DOI: will be inserted by hand later)

An *XMM-Newton* look at the Wolf-Rayet star WR 40⋆

The star itself, its nebula and its neighbours

E. Gosset **, Y. Nazé ***, J.-F. Claeskens, G. Rauw **, J.-M. Vreux, and H. Sana ***

Institute of Astrophysics and Geophysics, University of Liège, Allée du 6 août 17, B-4000 Liège, Belgium

Received; accepted

Abstract. We present the results of an *XMM-Newton* observation of the field of the Wolf-Rayet star WR 40. Despite a nominal exposure of 20 ks and the high sensitivity of the satellite, the star itself is not detected: we thus derive an upper limit on its X-ray flux and luminosity. Joining this result to recent reports of a non-detection of some WC stars, we suggest that the X-ray emission from single normal Wolf-Rayet star could often be insignificant despite remarkable instabilities in the wind. On the basis of a simple modelling of the opacity of the Wolf-Rayet wind of WR 40, we show that any X-ray emission generated in the particular zone where the shocks are supposed to be numerous will indeed have little chance to emerge from the dense wind of the Wolf-Rayet star. We also report the non-detection of the ejecta nebula RCW 58 surrounding WR 40. Concerning the field around these objects, we detected 33 X-ray sources, most of them being previously unknown: we establish a catalog of these sources and cross-correlate it with catalogs of optical/infrared sources.

Key words. stars:individual: WR 40 – stars: early-type – stars: Wolf-Rayet – X-rays: stars – ISM:individual: RCW 58 – ISM: bubbles

1. Introduction

Since the detection with the *EINSTEIN* satellite of X-ray emission originating from O stars in the Cyg OB2 association (Harnden et al. 1979), and from O stars as well as from a Wolf-Rayet (WR 25) in the Carina region (Seward et al. 1979), massive OB and Wolf-Rayet (WR) stars appeared to constitute a new class of rather moderate X-ray sources. Seward & Chlebowski (1982) further extended the list of O stars for the Carina region, also adding a second WR (WR 22). Subsequent studies using *EINSTEIN* (e.g. Pollock 1987) and *ROSAT* (e.g. Pollock et al. 1995) showed that X-ray emission from early-type stars (OB and WR) is a common phenomenon.

In the quest for the physical origin of this emission, two different categories of models have been proposed. In the so-called coronal model, Cassinelli & Olson (1979) introduced the existence of a coronal region at the base of the wind. This model had the advantage of explaining the observed high ionization (e.g. O VI lines) in OB supergiants by invoking the Auger effect. However, X-rays emitted from the base of the wind are strongly absorbed (see Cassinelli et al. 1981). Waldron (1984) proposed a solution to alleviate the problem by reducing the wind opacity to X-rays, but coronal models in general are subject to major criticisms (see Baade & Lucy 1987).

The second proposed mechanism is based on shock heated plasmas permeating the wind. Indeed, since the work of Lucy & Solomon (1970) and of Lucy & White (1980), it is clear that radiatively driven winds (which are now thought to be omnipresent in massive stars) exhibit intrinsic instabilities as the mechanism of momentum transfer is due to line absorption. As a result, inhomogeneities and shocks can form in these winds. According to Lucy & White (1980), these chaotic flows with blobs can be at the origin of an X-ray emission although the latter is bound to remain relatively faint. Lucy (1982) introduced the idea that blobs might evolve at different velocities due to reciprocal shadowing, thus creating forward shocks. These ideas have been further developed, particularly using recent hydrodynamical simulations. One-dimensional hydro-simulations revealed first the existence and strength of reverse shocks (Owocki et al. 1988) leading to a complex wind structure with clumps of dense material bounded on the inside by a reverse shock and on the outside by a possible weaker forward shock. Feldmeier et al. (1997b) further

Send offprint requests to: E. Gosset

⋆ Based on observations with *XMM-Newton*, an ESA Science Mission with instruments and contributions directly funded by ESA Member States and the USA (NASA).

** Research Associate FNRS, Belgium
*** Research Fellow FNRS, Belgium

elaborated that the X-ray production can be better explained by the clump collisions that are predicted by the 1-D simulations. The detailed applicability of these results to the actual physical (3-D) process remains unclear but model computations predict shock velocity jumps ranging from 500 to 1000 km s^{-1}, implying post-shock temperatures which could explain the observed thermal X-ray production of O stars. Runacres & Owocki (2002) investigated the propagation of inhomogeneities further out in the wind suggesting that the bulk of the X-ray emission could not originate from these distant regions.

From the observational point of view, Berghöfer et al. (1997) showed that the emission of X-rays from OB stars is a widespread phenomenon. They derived a typical luminosity L_X over L_{bol} ratio of 10^{-7}, but exhibiting a significant dispersion. It is nowadays well established that the X-ray emission from single early-type stars mainly consists of thermal emission from plasmas at a few million Kelvin (kT < 1 keV) located within the stellar wind. Recent studies on ζ Pup (O4Ief) with *XMM-Newton* (Kahn et al. 2001) and *Chandra* (Cassinelli et al. 2001) as well as on 9 Sgr (O4V) with *XMM-Newton* (Rauw et al. 2002) rather suggest that the thermal component is predominantly produced at distances between a few stellar radii R_* (even less than 1.2 R_* from the centre of the star according to Cassinelli et al. 2001) and up to 10-20 R_* but can be found throughout the wind. This result is in good agreement with wind shock models except for the strong shocks deeply embedded in the wind as reported by Cassinelli et al. (2001). However, the success of wind distributed shocks for interpreting sources like ζ Pup cannot be securely extended to all the stars of this class. A few anomalies persist for e.g. ζ Ori (O9.7Ib, Waldron & Cassinelli 2000), a significant one being the observed symmetry of the X-ray emission-line profiles. The same anomaly exists for δ Ori A (O9.5II, Miller et al. 2002), but this star also deviates by the narrowness of the X-ray lines compared to the terminal velocity of the wind. Even worse, τ Sco (B0.2V) shows evidence for infalling clumps and/or confined winds (Mewe et al. 2003, Cohen et al. 2003) which, although being mechanisms for producing shocks, represent a significant departure from the standard picture of outflowing gas.

For the sake of completeness, one should point out that some stars which have a population of relativistic electrons can exhibit a non-thermal component supposed to be produced by inverse Compton scattering (Chen & White 1991). Some other stars exhibit much higher X-ray luminosity than expected from their L_{bol} and the 'canonical' 10^{-7} ratio. This is usually attributed to an interaction of the winds in massive double systems. Indeed, Cherepashchuk (1976) and Prilutskii & Usov (1976) developed the idea that the supersonic winds of massive early-type stars in double systems collide and will generally produce an additional X-ray source on top of the individual ones (see Luo et al. 1990, Stevens et al. 1992, Pittard & Stevens 1997, 2002). This additional emission, depending on the distance between both stars and on the relative strength of their winds, is expected to be at least partly harder than the emission of single stars.

The situation is much less clear concerning WR stars. Since the *EINSTEIN* detection and later work by Pollock (1987), several studies took place (see also, using *ROSAT* data, Pollock et al. 1995). They suggested that: 1) single WN stars are, on average, X-ray brighter than single WC stars, 2) WR+OB binary systems tend to be brighter than isolated stars and 3) the few WR stars with absorption lines in their spectra appear significantly X-ray brighter than average single stars (an indication that they could be multiple). Unlike what was obtained for OB stars, Wessolowski (1996) found no clear cut relationship between L_X and L_{bol} from ROSAT observations of 41 WN type stars.

Interestingly, a recent *XMM-Newton* observation of WR 114 (WC5) by Oskinova et al. (2003) failed to detect the star. The authors conclude that the conspicuous absence of the star in the X-ray image gives an upper limit to the X-ray luminosity of $L_X < 2.5\ 10^{30}$ erg s^{-1} and a ratio L_X over L_{bol} less than $4\ 10^{-9}$. They also present other examples of non-detection of WC stars concluding that single WC stars should not be detected in the X-ray domain due to the large opacity of their winds, further stating that all WC stars detected are currently known to be in binary systems (e.g. γ Vel, see Skinner et al. 2001). This indeed suggests that the observed X-ray emission originates from some interaction phenomenon between the two components and is not an intrinsic property of the WC stars.

With the aim of studying the X-ray emission of a single WR star, Skinner et al. (2002a) observed WR 110 (WN5) which was certainly not suspected to be in a binary system. They report a dominant contribution from a mildly cool plasma at $kT = 0.5$ keV. The interesting point is that no excess absorption over the interstellar column is present in front of this rather cool component. This indicates that the emission could not be produced deep in the wind of the WR star. A hot component is also present in WR 110 which is also hard to interpret. These two characteristics are however easily explained if one admits that WR 110 is actually a hidden binary system.

The brightest WN star in the X-ray domain is WR 25 (WN7+abs). Its status has induced a lot of interest. A recent study showed that the corresponding X-ray emission of WR 25 is made of a cool component at $kT = 0.55$ keV and of a hot component (Raassen et al. 2003). Both components are absorbed, the largest column being in front of the cool component. If the cool component can be explained by instabilities in the wind, the hot one is here again difficult to explain in the same way and is conventionally associated to processes like colliding winds. The similarity with WR 110 is rather strong. However, the possibility that WR 25 be a binary has to be corroborated by other means. Despite the presence of absorption lines in its spectrum, all attempts to prove the binarity of WR 25 by other means have failed until now. The mere existence of absorption lines of hydrogen in the spectrum is definitely

not a proof. Indeed, the corresponding lines have been observed in the massive WR+O binary WR 22 (WN7+abs + O6-9 III-V) and these lines have been shown to belong to the WR component (Rauw et al. 1996).

In the framework of the GT time of the Optical Monitor consortium on *XMM-Newton*, we observed WR 22. The low-resolution X-ray spectrum is very similar in shape to the one of WR 25 with the two components, a cool one and a hot one (see preliminary results in Gosset et al. 2003; see also Gosset et al. in preparation). Clearly the situation is dominated by a colliding wind phenomenon, which was in this case expected. These results suggest that WR 25 could indeed be another hidden binary system.

Finally, in a recent paper, Skinner et al. (2002b) report X-ray observations of WR 6 (EZ CMa, WN4, SB1?) whose binary nature has been the most debated among WR stars. A periodic modulation (P=3.765 days) of the optical luminosity and of the spectrum of WR 6 remained over decades. The spectral features have been studied in detail and they turned out to exhibit variations that are rather well interpreted by Corotating Interacting Regions (see e.g. Dessart & Chesneau 2002). Again two components (a cool one at $kT = 0.59$ keV, a hot one at $kT = 3.5$ keV) are present in the X-ray spectrum and Skinner et al (2002b) point out the great similarity between WR 110 and WR 6. Of course, the problem of the interpretation of the hot component remains. The similarity of the spectrum with the one of WR 22 is also striking.

Quite recently, Ignace et al. (2003) reported on *XMM-Newton* observations of the WR star WR 1 (WN4). Although the star is detected, the hot component seems to be absent or at least comparatively much cooler. Ignace et al. (2003) also tentatively reported the detection in the X-ray spectrum of absorption features, interpreted as being due to K-shell absorption edges of N and Si. They argued that WR 1 is probably single contrary to WR 6 and WR 110.

All the above-mentioned studies show that the X-ray emission from WR stars is far from being a fully understood phenomenon. This partly results from the still fragmentary knowledge we have of the WR wind structure and properties. In an attempt to shed some light on this subject, we decided to observe WR 40 with the *XMM-Newton* observatory. In the framework of the GT time of the Optical Monitor consortium, we acquired a 20 ks exposure on WR 40 (WN8). The motivations behind the choice of this target and related information can be found in Sect. 2. In Sect. 3, we give the details on the *XMM-Newton* observations and on the corresponding reductions. Sect. 4 reports the absence of detection of the star. In Sect. 5, we address the possibility, through simple modelling, that the non-detection could be due to the optical depth of the wind. Section 6 deals briefly with the ejecta nebula RCW 58 surrounding WR 40. Finally, Sect. 7 is devoted to the search for other X-ray sources around the position of WR 40 and a first catalog of sources is established. The conclusions of our work are given in Sect. 8.

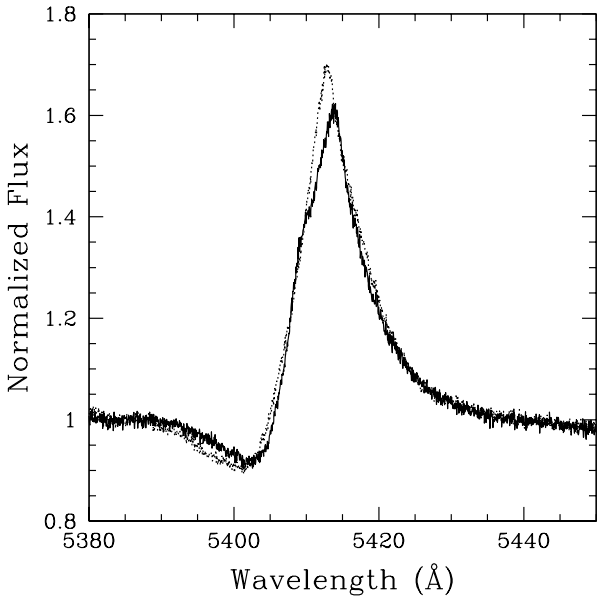

Fig. 1. The profile of the He II λ5412 line in the spectrum of WR 40. The two spectra were acquired with the ESO 1.5m + FEROS on two consecutive nights in May 1999; they are normalized to the continuum. The variability is clear and is always present on such a short time-scale.

2. Characteristics of WR 40

WR 40 (≡ HD 96548) is the optically brightest WN8 in the sky. With a peak to peak amplitude of 0.1 mag, it is also one of the photometrically most variable ones (Lamontagne & Moffat 1987). The debate on the presence of deterministic variations in the photometry is, in our opinion, still open (Smith et al. 1985, Gosset et al. 1989, Balona et al. 1989, Gosset & Vreux 1990, Matthews & Moffat 1994, Antokhin et al. 1995, Marchenko et al. 1998). Although WR 40 is considered to be a single star, its spectrum is extremely complex as well as strongly variable (see a first study by Moffat and Isserstedt 1980). Several years ago, WR 40 was regularly mentioned in the literature as a good representative candidate of the WR + compact companion evolutionary status (see e.g. Cherepashchuk & Aslanov 1984). We initiated some time ago a photometric and spectroscopic monitoring of this star: the results will be reported elsewhere. We just illustrate in Fig. 1 the strong variability of the emission lines. Figure 2 demonstrates that variable features are sometimes visible in the absorption components of P Cygni profiles. All these characteristics are quite concordant with what is expected from an inhomogeneous, perhaps unstable, wind, although a direct relation between the spectroscopic observations and the specific theoretical models is always difficult to establish.

Recently, a tailored analysis of the ultraviolet to infrared spectrum of WR 40 has been performed using the so-called standard model. The latter consists in line-

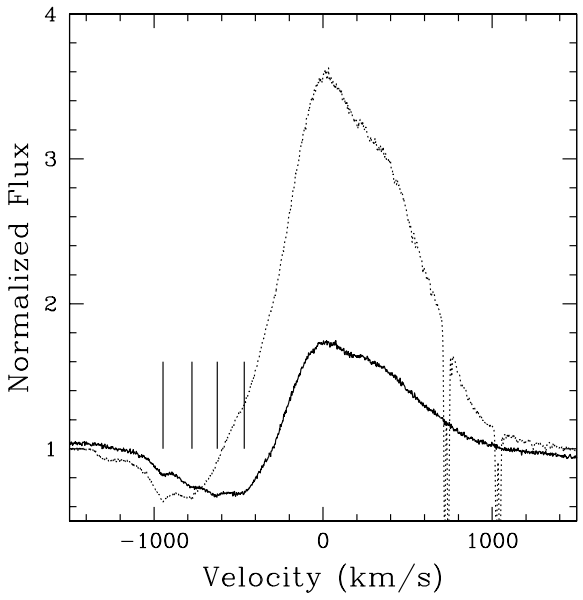

Fig. 2. The profiles of two different He I lines (continuous line: He I λ4471; dotted line: He I λ5876) as observed in a single spectrum of WR 40 acquired with the ESO 1.5m + FEROS in May 2000. At that time, the emission component was appearing double in velocity. More interestingly, a transient pattern is visible in the absorption component of the P-Cygni profiles. It suggests a set of localized enhanced absorptions at various velocities; vertical ticks underline the phenomenon. These absorption features are undoubtedly real, since the S/N ratio of the spectrum exceeds 100 in these wavelength regions. This observation is strongly suggestive of the existence of wind inhomogeneities.

blanketed non-LTE model atmospheres with provisions for a clumped wind. We thus have at our disposal a model atmosphere and a set of values for the physical parameters characterizing this star (Herald et al. 2001).

Therefore, WR 40 appears as an interesting and very promising object in order to widen the parameter space of WRs covered by recent sensitive X-ray observations. It is also considered as a good candidate to detect the possible X-ray component due to line-driven wind instabilities.

3. Observations and data reduction

The WR 40 field was observed with the *XMM-Newton* observatory (Jansen et al. 2001) during revolution 405 on February 23–24, 2002 (pointing 0109280101, HJD 2 452 329.49766–HJD 2 452 329.77459). The two EPIC-MOS instruments were operated in the full frame mode (Turner et al. 2001) whilst the EPIC-pn camera was used in the extended full frame mode (Strüder et al. 2001). All three EPIC instruments used the thick filter to reject UV/optical light from the target. We used version 5.3.3 of the *XMM-Newton* Science Analysis System (SAS) to reduce the raw EPIC data. For the MOS instruments, we filtered the event list to select only events with patterns in the range 0–12 and complying with the selection criterion XMMEA_EM. For the pn detector, we restricted ourselves to one and two photon events (patterns 0–4) and to a flag of zero. On the basis of the inspection of particular patterns (e.g. 26–29) but also on the observed count rates (see below), we conclude that no pile-up is apparent in the present data. During the exposures, weak proton flares occurred. Although the approach can be questioned for bright sources (see the discussion in De Becker et al. 2004), we chose to reject the associated bad time intervals from any further analysis since most of the sources are rather weak (see below). The intervals were considered as bad if the count rates of events above 10 keV (actually with pattern 0 and pulse invariant PI > 10000) were in excess of 0.25 counts s^{-1} for the EPIC-MOS detectors and in excess of 1.0 counts s^{-1} for the EPIC-pn one. Resulting effective exposure times were reduced to 19 482 s, 19 673 s and 12 043 s for MOS1, MOS2 and pn, respectively; these values correspond to the central part of the field (extraction region). We built images using the EVSELECT task in three bandpasses 0.5–1.5 keV (soft), 1.5–2.5 keV (medium) and 2.5–10 keV (hard) plus the total 0.5–10 keV (total) domain. We preferred to neglect photons below 0.5 keV owing to the relatively large uncertainties on the calibrations in this range of energy. The positions of the events were binned; we selected a pixel size of about 2.″5. This operation was performed for the three instruments independently. We also merged the event lists of the different instruments in order to create a combined image. A false-colour image (three basic colours) of the entire field is given in Fig. 3. WR 40 is situated at the centre of the field and is conspicuously absent. A very few soft sources are clearly present, two being at the edge of the observed field. Several other sources, much harder (i.e. blue), are also visible near the central part of the field. Figure 4 (left panel) zooms in on the central field where WR 40 should have been detected; the total bandpass (0.5–10 keV) is used. Again, no trace of WR 40 is present. We performed the same search in the different individual bandpasses with the same lack of success. To further ascertain the non-detection of WR 40, we checked carefully the astrometric calibration of the field. The identification of another bright source in the field with HD 96309 is quite secure (see Sect. 7.2) and further confirms the expected position of the Wolf-Rayet star. Finally, we smoothed the X-ray image using a gaussian function with $\sigma = 3$ pixels. A background fluctuation has its maximum some 2″ to the NW of the position of WR 40 (see Fig. 4 right panel). This fluctuation is too small to be significant and thus to be associated with an existing source. It is mainly originating from the MOS2 image. In addition, we tried to adjust to the image the theoretical point spread function (psf) using the task EMLDETECT forced at the expected position of WR 40. We also performed the same procedure at random positions in the field. Indeed, several fluctuations of similar amplitude can easily be spotted in the smoothed image of the field. No adjustment of the psf at the position of WR 40 turned out to be systematically more significant

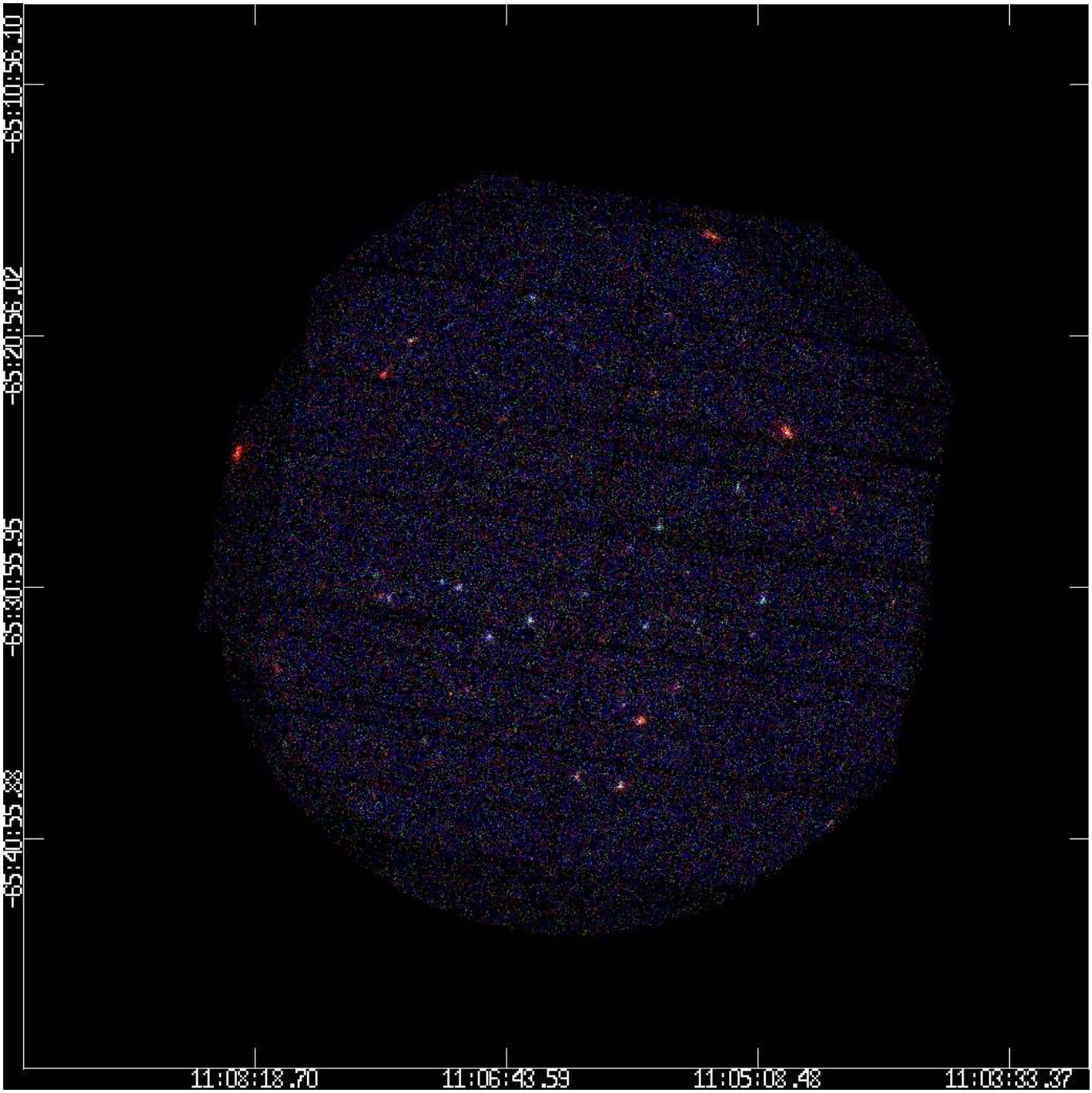

Fig. 3. The combined three instrument X-ray image of the WR 40 field. Shown is a false-colour image where the three different colours correspond to different bandpasses (red: soft, green: medium, blue: hard). The full field of view is about 30′ in diameter. A few bright, rather soft sources are visible as well as several hard ones, particularly in the southern part of the field. The centre of the field is pointing at WR 40 which is not seen: it is located at α(J2000) = $11^{\rm h}\ 06^{\rm m}\ 17\overset{\rm s}{.}2$ δ(J2000) = –65° 30′ 35″ .

than those issued from the random positions. Therefore, we can already conclude that WR 40 is not detected in this *XMM-Newton* observation.

4. Results: the non-detection of WR 40

The absence of WR 40 in the X-ray images must be quantified as accurately as possible through the determination of an upper limit for the count rates. We estimated the background at the expected place of WR 40 by integrating the number of events in circles of different radii. Fluctuations from circle to circle are quite compatible with Poisson statistics. The only marked deviation concerns the MOS2 detector and small circles of radii around 4-5″. Typically, the expected counts are 1 or less and the observed ones are 4-5 (all in the hard band). This remains marginal, small number statistics and the effect is not present in the two other detectors. This corresponds to the fluctuation men-

Table 1. For each of the three individual detectors, as well as for the combined EPIC image, we give, for the locus of WR 40, the value in counts of the background, the critical counts corresponding to the maximum poissonian fluctuations corresponding to a logarithmic likelihood of 12, the resulting net maximum counts for a possible source at the detection threshold and the corresponding count rate corrected for the psf outside the detection area. These values are given for the three energy bands considered (soft: 0.5–1.5 keV, medium: 1.5–2.5 keV, hard: 2.5–10 keV) as well as for the total one (0.5–10 keV); we also consider both basic detecting square areas (5 pixels by 5 pixels and 3 pixels by 3 pixels, the pixels having sizes of $2\farcs5$).

		5 × 5				3 × 3			
Detector		Soft	Medium	Hard	Total	Soft	Medium	Hard	Total
MOS1	Background counts	0.9	0.8	1.0	2.7	0.3	0.3	0.4	1.0
	Critical counts	7.9	7.3	8.2	12.8	5.5	5.1	5.6	8.1
	Net maximum counts	7.0	6.6	7.2	10.2	5.1	4.9	5.3	7.1
	Maximum Count Rate (10^{-4} s^{-1})	8.0	7.5	8.3	11.6	8.8	8.4	9.1	12.2
MOS2	Background counts	1.1	0.6	1.9	3.6	0.4	0.2	0.7	1.3
	Critical counts	8.5	6.7	10.9	14.9	5.8	4.7	7.1	9.1
	Net maximum counts	7.4	6.1	9.0	11.3	5.4	4.5	6.4	7.9
	Maximum Count Rate (10^{-4} s^{-1})	8.4	6.9	10.2	12.8	9.2	7.7	10.9	13.3
pn	Background counts	1.1	1.2	3.6	5.8	0.4	0.4	1.3	2.1
	Critical counts	8.4	8.7	14.9	19.4	5.7	5.9	9.1	11.4
	Net maximum counts	7.4	7.6	11.3	13.6	5.4	5.5	7.9	9.3
	Maximum Count Rate (10^{-4} s^{-1})	13.6	14.0	20.9	25.2	14.8	15.3	21.7	25.7
EPIC	Background counts	3.0	2.5	6.5	11.9	1.1	0.9	2.3	4.3
	Critical counts	13.7	12.4	20.7	30.3	8.5	7.9	12.0	16.5
	Net maximum counts	10.7	9.9	14.3	18.3	7.5	7.0	9.7	12.2
	Maximum Count Rate (10^{-4} s^{-1})	4.6	4.3	6.2	8.0	4.9	4.5	6.3	7.9

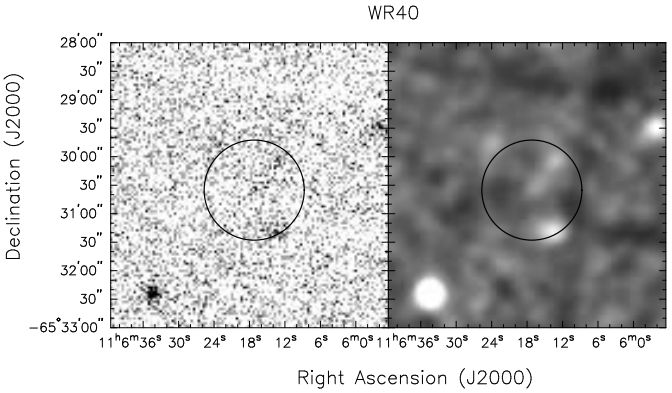

Fig. 4. The central part of the X-ray image in the total energy band obtained by combining the three EPIC instruments. The position of WR 40 is at the centre of the circle ($52''$ radius). Left panel: the basic image built with $2\farcs5$ pixels. Right panel: a smoothed version of it with an inverse gray-scale. Using the internal source numbers as defined in Section 7.1 (see also the catalog in Table 5), the source at the bottom left is recognized as being source #22, the source at the upper right is source #15. The faint source on the circle (bottom) is source #18. The linear dark streaks visible in the right panel correspond to CCD gaps and bad columns.

tioned in the previous section. The adopted final values for the background rely on a circle of radius $24\farcs75$. The detection of source candidates by the task EBOXDETECT is usually done on a basic square area of 5 × 5 or 3 × 3 image pixels: these box square areas correspond to angular sizes of $12\farcs5$ by $12\farcs5$ or $7\farcs5$ by $7\farcs5$, respectively. These sizes are rather well adapted to our aim since the full width at half maximum of the central parts of the EPIC psf's is about $5''$. We indeed expect the detection of a source to be due to this central part of the psf and not to the much larger halo. In Table 1, we report the estimated counts in the background as converted for these square box areas (5 pixels × 5 pixels and 3 pixels × 3 pixels, respectively), for the different bandpasses and the different instruments. Poisson fluctuations are expected in these areas: we accept them up to some level above which we must attribute the apparent fluctuation to the detection of a source. We chose a count threshold corresponding to a logarithmic likelihood of 12 (this logarithmic likelihood translates into a value of $6.1\,10^{-6}$ for the probability under the null hypothesis of pure background fluctuations to observe a count in excess of this given critical value). The formal Poisson count (not necessarily an integer) used as a threshold, the so-called critical value, is given in every second line of Table 1. The third line gives the background corrected count and the fourth line the resulting count rates which will be used as upper limits. To obtain these values, we first subtracted the background from the threshold count and then divided the background corrected count by the exposure time as deduced for the location of WR 40 in the field. We further multiplied the count rate by a correcting factor that takes into account the fact that the square area does not contain the whole psf. From the *XMM-Newton* users' manual, we estimated the percentage of the counts in the basic square area as 45 % (5 × 5) and 30 % (3 × 3) of the full psf, and we neglected here the energy dependency of this correction. The same steps have been followed for the combined image of the three instruments. The resulting counts are the mere sum of the individual ones (to preserve poissonian statistics). The exposure time is the cumulated one

(i.e. 51 198 s). The corresponding values are given in Table 1 under the label EPIC.

We also derived an independent value of the upper limit on the count rate for WR 40. This value is computed on the basis of the search for other sources in the field (see Sect. 7.1) and the upper limit is estimated from the faintest detected sources. The search is performed simultaneously over the three energy bands and the three instruments. The resulting values (details are given in Sect. 7.1) correspond to 5 10^{-4} counts s^{-1} for each MOS detector and to 1 10^{-3} counts s^{-1} for the pn detector. These values combine to give 6.2 10^{-4} counts s^{-1} for the EPIC instrument and are in very good agreement with the values derived in Table 1 (entries Total and EPIC). It is also interesting to notice that the limit (maximum) count rates given in Table 1 under the label 5 × 5 and under the label 3 × 3 are quite similar; this means that the adopted limit count rate is not too dependent of the characteristics of the basic detecting area.

5. Towards an interpretation

The non-detection of WR 40 in the X-ray domain implies either that the star does not produce enough X-ray emission at any place in the wind due to a particular behaviour of the WR winds (at least those of WN8 stars) compared to O-star ones, or that the X-ray emission is naturally generated deep enough in the wind to be unable to emerge out of it. In order to further test these ideas, we must estimate the effect of the wind opacity on the X-ray radiation in the particular case of WR 40.

5.1. A model for the wind opacity

Clearly, the matter close to an early-type star is subjected to the stellar radiation field and is thereby ionized. The effect of the ionization structure could be important and it is therefore conceptually not correct to naïvely use, for a wind absorbing column, the same model as for the neutral interstellar medium. Several authors (e.g. Krolik & Kalman 1984, Waldron 1984) have demonstrated that a comprehensive study of the X-ray throughput from massive stars required a detailed modelling of the opacity from such an ionized wind. We have thus attempted to model the wind opacity of WR 40.

We have considered the 10 most abundant elements (H, He, C, N, O, Ne, Mg, Si, S, Fe) whose abundances were fixed to the ones obtained by Herald et al. (2001) in their tailored analysis of WR 40. In our model, only the collisional excitation, the photoionization, and the radiative and dielectronic recombinations can affect the ionization level of the elements. Collisional excitation rates were taken from Voronov (1997), and the photoionization cross-sections from Verner et al. (1996) for the outer shells and Verner & Yakovlev (1995) for the inner shells. Since inner-shell ionization can lead to the ejection of multiple electrons, we used the probability distribution of the number of ejected electrons from Kaastra & Mewe (1993)

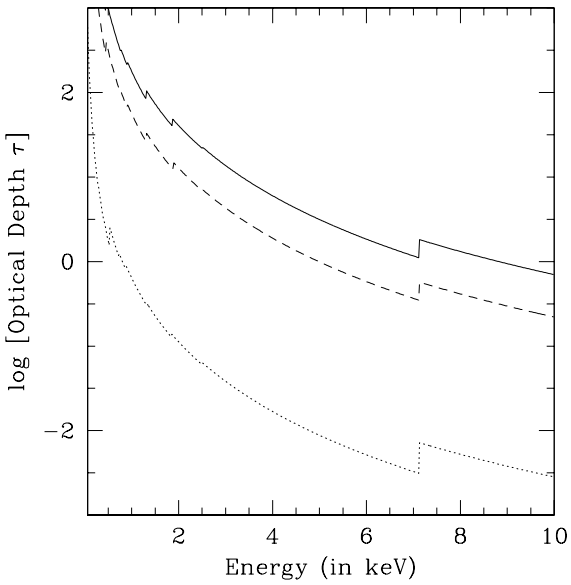

Fig. 5. Logarithm of the optical depth in the X-ray domain of the wind of WR 40 from 5 R_* outwards. The solid line corresponds to the smoothed mass-loss rate $\dot{M}_{\rm sm} = 10^{-4}$ $M_\odot$ yr^{-1}, and the dashed one to the clumpy mass-loss rate $\dot{M}_{\rm cl} = 3.2\,10^{-5}$ $M_\odot$ yr^{-1}. The dotted line corresponds to the optical depth of a neutral hydrogen column of $N_{\rm H} = N_{\rm H\,I} + 2 \times N_{\rm H_2} = 2.6\,10^{21}$ cm^{-2} (Herald et al. 2001).

to model this effect for the elements considered above. Radiative and dielectronic recombination rates were taken from Verner & Ferland (1996), Aldrovandi & Péquignot (1973), Woods et al. (1981) and Shull & van Steenberg (1982), taking into account the corrections for the last reference as suggested by Arnaud & Rothenflug (1985).

We determined the ionization structure of the wind up to some 300 stellar radii (with a logarithmic spatial bin from 5 R_* to 321 R_*), using the approximations of Waldron (1984) for the radiation field (his eq. 12) and for the opacities (his eqs. 13 and 14). However, we chose to fix the velocity law and the wind temperature. We adopted $v(r) = v_0 + v_\infty\,(1 - \frac{R_*}{r})$, with $v_0 = 10$ km s^{-1}, $v_\infty = 840$ km s^{-1}, and $R_* = 10.6$ $R_\odot$ and $T_{\rm wind}(r) = T_\infty + (T_0 - T_\infty)\,(\frac{R_*}{r})^{1.9}$ with $T_0 = T_* = 45\,000$ K and $T_\infty = 0.4 \times T_0$ (see Lamers & Morris 1994). The stellar parameters were taken from Herald et al. (2001) except for v_0. The stellar continuum flux, from UV to IR, was calculated as in Rauw (1997) for the same set of stellar parameters, as well as for the same temperature and velocity laws, while the local emission was approximated by a simple blackbody at $T_{\rm wind}$.

We performed the model computations for two different mass-loss rates (see Herald et al. 2001): the smoothed mass-loss rate which amounts to $\dot{M}_{\rm sm} = 10^{-4}$ $M_\odot$ yr^{-1}, and the one labelled clumpy which is $\dot{M}_{\rm cl} = 3.2\,10^{-5}$ $M_\odot$ yr^{-1}. The clumpy case is given for comparison to estimate the effect of the adopted mass-loss rate. In Fig. 5,

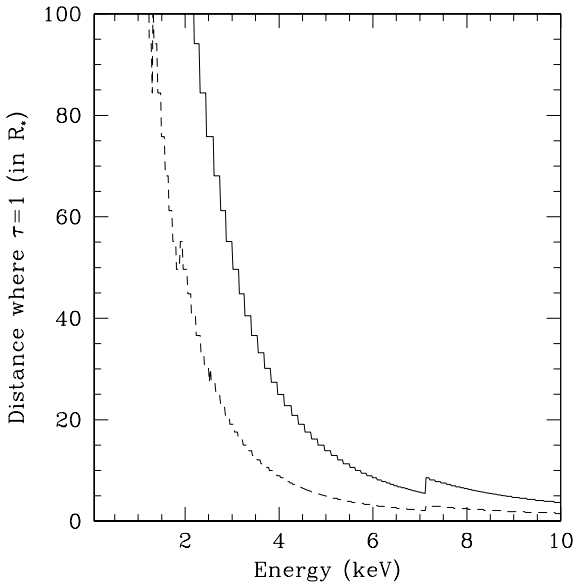

Fig. 6. Distance from the star (in stellar radii) where the X-ray optical depth τ_x equals 1. The solid line corresponds to the smoothed mass-loss rate whereas the dashed line corresponds to the clumpy one.

we show the resulting optical depth for the wind of WR 40 as a function of the energy; the interstellar optical depth is given for comparison. In Fig. 6, we plotted the distance from the star where the X-ray optical depth is unity (τ_x = 1). It is immediately clear that the wind optical depth of WR40 is incredibly large, even far from the star. As a consequence, in order to be observed, the flux in the soft band must predominantly form at large radii. Indeed, if the emitting plasma is deeply embedded in the wind, all the flux below 1 keV (for the clumpy case) or 2 keV (for the smoothed one) is completely absorbed. Any possible emerging X-ray emission is thus bound to be markedly harder than the one intrinsic to the emitting plasma.

We also tried to evaluate the count rates expected for WR 40 when using the *XMM-Newton* satellite. To this aim, we used the XSPEC (version 11.2.0) task FAKEIT with the combined rmf+arf matrices (available from the SOC, release of June 2001). We introduced in XSPEC (version 11.0.1) new multiplicative table models similar to the built-in *wabs* but taking into account the opacities for the WR wind as calculated above. Hereafter, the description of our results is limited to the smoothed mass-loss rate. We also restricted the set of models to optical depths above a certain set of radii (see below). This use of XSPEC allows us to compute emergent fluxes provided that we have a model for the emitting plasma.

5.2. An approximation for the emergent flux

In order to model the flux that could emerge from the Wolf-Rayet star, we first imagined which kind of emission could be generated, and subsequently applied the opacity effect of the wind. Since we have no information on the possible source of X-ray emission that we should associate with WR 40, we had to tentatively select a family of reasonable models. We chose three optically thin thermal plasma models that span a large variety of possibilities. We used the MEKAL formalism (Mewe et al. 1985, Kaastra 1992) to model the thermal plasmas and we fixed the temperature of the first model (A) to 0.6 keV. We attributed to the emitting plasma the same abundances as those reported for WR 40 by Herald et al. (2001). Model B is similar but with a temperature kT = 1.2 keV which can probably be considered as extreme for a single early-type star. Finally, we chose as Model C the characteristics of the plasma observed for the brightest X-ray emitter presently known among the WN stars i.e. WR 25 (model 12, table 6 from Raassen et al. 2003). The latter is characterized by a two-temperature plasma (kT_1 = 0.61 keV, kT_2 = 2.83 keV). We fixed the ratio of the emission measures of the two components to the value derived for WR 25, and modelled the emitting plasma by two MEKAL components with the abundances of WR 25 (see Raassen et al. 2003). The three models of X-ray emitters have been put below wind layers at different depths. In other words, the intrinsic unabsorbed X-ray emission has been located in a thin narrow shell positioned either directly below a radius of 1.5 R_*, or directly below 5 R_*, or directly below 21 R_* or directly below 105 R_*. Only the absorption by the part of the wind situated above respectively 1.5 R_*, 5 R_*, 21 R_* or 105 R_* has thus been taken into account. All these distances are counted from the star centre. For the sake of completeness, we also positioned the models outside the wind, just taking into account the interstellar extinction alone. Our model is simple and thus illustrative. The four selected locations for the X-ray emitting plasma represent the minimum set of values necessary to sample the wind on a logarithmic scale. In the framework of the present knowledge of shocked winds, they can be somewhat related to remarkable features. The first step (1.5 R_*) limits the zone where a possible corona is expected; very few shocks are expected so deep in the wind, at least for O stars (Feldmeier et al. 1997a, Rauw et al. 2002, Kahn et al. 2001, Cassinelli et al. 2001, Runacres & Owocki 2002). The zone at 5 R_* is the expected location of strong shocks in O-type stars (Feldmeier et al. 1997b) whereas 21 R_* represents the typical upper limit on the observed region of X-ray line emission. Finally, 105 R_* is representative of the outer wind, a region beyond which no significant amount of hot gas should exist (Runacres & Owocki 2002). Of course, such a model is meaningful only if the hot gas emits X-ray radiation in place before being further transported with the wind. The radiative cooling time must be inferior to the flow time. For O stars, this is certainly the case for the inner wind up to a few tens of stellar radii; this should even be true further out for WR stars (Hillier et al. 1993, Feldmeier et al. 1997a). We made an estimation of the cooling time in the particular case of WR 40. Assuming the expression for cooling time

as given by equation 6 of Stevens et al. (1992) and the total X-ray cooling rates associated to WN stars as given by their figure 10 (10^{-23} erg cm^3 s^{-1}), we find typical cooling times of ∼1200 s (0.6 keV, Model A) to ∼2700 s (1.2 keV, Model B) at 21 R_*. At the same position in the wind of WR 40, the flow takes 9000 s to travel over one stellar radius, leading to a ratio between the flow time and the cooling time of at least 3. The situation is still more favourable deeper in the wind, the ratio reaching 5000 at 1.5 R_*. Therefore, the cooling can be considered as almost instantaneous in the inner wind regions. At 105 R_*, the cooling time amounts to ∼31000 s (Model A) and to ∼69000 s (Model B) which corresponds to the time necessary for the flow to travel over 8 R_*. Clearly, the approximation of instantaneous cooling is still rather valid in these outer layers of the wind.

Table 2 gives, for the different bandpasses, the different models and the different locations of the emitting plasmas in the wind, the fraction of the intrinsic flux of X-ray emission that emerges from the wind. From an inspection of Table 2, it is further confirmed that the soft band and to some extent the medium band contribute little to the total flux. Most of the signal is due to the hard band as long as the emitting plasma is below 21 R_*. Even if the plasma is situated just below 105 R_*, the outgoing X-ray emission is still slightly harder compared to the intrinsic emission. In this respect, it is interesting to notice that, for Model B for example, in the total band (0.5–10 keV), only 9 per cent of the flux ($1 - \frac{0.151}{0.165}$) is absorbed by the interstellar medium whereas 34 per cent ($1 - 0.66$) of the intrinsic flux of Model B would have been absorbed without the effect of the wind. This simple example illustrates the impact of the hardness of the X-ray emission on the correction for extinction. The fractions of emerging flux given in Table 2 are in good agreement with the indications given by Figs. 5 and 6. Some flux in the medium and soft bands could be present if the hot plasma exists up to several tens of stellar radii.

In order to give an idea of what could be detected with *XMM-Newton*, we have to estimate count rates corresponding to the different models. In this context, we have to imagine which amount of matter is emitting in the X-ray domain. Indeed, the basic flux is proportional to the intrinsic emissivity of the model of plasma multiplied by the emission measure (EM). The EM expressed in cm^{-3} is related to the norm used in XSPEC through the following equation

$$N = \frac{10^{-14}}{4\pi D^2} EM = \frac{10^{-14}}{4\pi D^2} \int_V n_{\rm e}\, n_{\rm H}\, dV$$

where the integral is taken over the volume and D is the distance to WR 40. Although the emissivity is fully determined by the model, the EM is fully arbitrary in the present case. In the context of our model, the relation between the count rates and the EM is basically linear, which gives sense to arbitrarily fixing the norm. Therefore, we decided to set the norm N (and thereby the EM) to the one observed for WR 25. For the latter, we have $N_1 = 5.816\,10^{-3}$ cm^{-5} (kT_1=0.61 keV) and $N_2 = 2.358\,10^{-3}$ cm^{-5} (kT_2=2.83 keV). We adopted these values for model C whereas we adopted the sum N_t=8.174 10^{-3} cm^{-5} for the single temperature models A and B. As the adopted distances to the two stars are quite similar, no effort has been made to take into account the exact difference in distance owing to the arbitrariness of the scale.

Table 2. Emerging flux as a fraction of the total flux emitted by the plasma. Every first line corresponds to the absorption by the wind alone whereas every second line also includes the effect of the interstellar medium (ISM). The extinction effect of the ISM alone is given in the second column. The results are given for the three energy bands considered and for the total one. Each subtable deals with a different model for the immersed thermal plasma (models A, B and C; see Sect. 5.2 for further details). No value is given when the fraction is smaller than 10^{-13}.

Model A (0.6 keV)					
Energy (keV)	ISM	< 1.5 R$_*$	< 5 R$_*$	< 21 R$_*$	< 105 R$_*$
0.5-1.5	0.45	–	–	$6.50\,10^{-9}$	0.0145
		–	–	$5.13\,10^{-9}$	0.0105
1.5-2.5	0.87	–	$5.88\,10^{-12}$	$7.19\,10^{-4}$	0.281
		–	$5.52\,10^{-12}$	$6.67\,10^{-4}$	0.248
2.5-10	0.96	$4.64\,10^{-6}$	$3.04\,10^{-3}$	0.101	0.672
		$4.62\,10^{-6}$	$3.02\,10^{-3}$	0.099	0.648
0.5-10	0.50	$5.63\,10^{-8}$	$3.68\,10^{-5}$	$1.29\,10^{-3}$	0.0496
		$5.60\,10^{-8}$	$3.65\,10^{-5}$	$1.26\,10^{-3}$	0.0424

Model B (1.2 keV)					
Energy (keV)	ISM	< 1.5 R$_*$	< 5 R$_*$	< 21 R$_*$	< 105 R$_*$
0.5-1.5	0.52	–	–	$1.57\,10^{-8}$	0.0256
		–	–	$1.24\,10^{-8}$	0.0187
1.5-2.5	0.88	–	$1.09\,10^{-11}$	$1.15\,10^{-3}$	0.303
		–	$1.02\,10^{-11}$	$1.07\,10^{-3}$	0.271
2.5-10	0.97	$1.22\,10^{-4}$	0.0237	0.205	0.738
		$1.21\,10^{-4}$	0.0235	0.202	0.718
0.5-10	0.66	$1.25\,10^{-5}$	$2.43\,10^{-3}$	0.0214	0.165
		$1.24\,10^{-5}$	$2.42\,10^{-3}$	0.0210	0.151

Model C (WR 25)					
Energy (keV)	ISM	< 1.5 R$_*$	< 5 R$_*$	< 21 R$_*$	< 105 R$_*$
0.5-1.5	0.42	–	–	$3.43\,10^{-9}$	0.0114
		–	–	$2.70\,10^{-9}$	$8.03\,10^{-3}$
1.5-2.5	0.88	–	$1.28\,10^{-11}$	$1.34\,10^{-3}$	0.301
		–	$1.20\,10^{-11}$	$1.24\,10^{-3}$	0.269
2.5-10	0.98	$7.18\,10^{-4}$	0.0709	0.340	0.801
		$7.15\,10^{-4}$	0.0706	0.337	0.785
0.5-10	0.56	$9.61\,10^{-5}$	$9.50\,10^{-3}$	0.0457	0.155
		$9.58\,10^{-5}$	$9.45\,10^{-3}$	0.0453	0.146

Table 3. Typical count rates as would be derived from *XMM-Newton* observations. The extinction due to the ISM is combined with the one due to the wind. The count rates are indicative and correspond to an arbitrarily chosen norm of $8.174\,10^{-3}$ cm^{-5} (see text). Conversion to other values for the norm is linear. See Table 2 for missing values.

Model A (0.6 keV)				
Energy (keV)	< 1.5 R$_*$	< 5 R$_*$	< 21 R$_*$	< 105 R$_*$
		MOS		
0.5-1.5	–	–	$3.85\,10^{-5}$	$1.36\,10^{-1}$
1.5-2.5	–	$2.52\,10^{-7}$	$4.86\,10^{-4}$	$2.31\,10^{-1}$
2.5-10	$5.46\,10^{-8}$	$9.02\,10^{-5}$	$5.35\,10^{-3}$	$4.13\,10^{-2}$
0.5-10	$5.47\,10^{-8}$	$9.06\,10^{-5}$	$5.90\,10^{-3}$	$4.23\,10^{-1}$
		pn		
0.5-1.5	–	–	$1.58\,10^{-4}$	$4.22\,10^{-1}$
1.5-2.5	–	$4.86\,10^{-7}$	$1.41\,10^{-3}$	$6.88\,10^{-1}$
2.5-10	$2.77\,10^{-7}$	$2.86\,10^{-4}$	$1.35\,10^{-2}$	$1.05\,10^{-1}$
0.5-10	$2.77\,10^{-7}$	$2.87\,10^{-4}$	$1.51\,10^{-2}$	$1.22\,10^{0}$
		EPIC		
0.5-1.5	–	–	$6.67\,10^{-5}$	$2.03\,10^{-1}$
1.5-2.5	–	$3.07\,10^{-7}$	$7.02\,10^{-4}$	$3.38\,10^{-1}$
2.5-10	$1.07\,10^{-7}$	$1.36\,10^{-4}$	$7.26\,10^{-3}$	$5.64\,10^{-2}$
0.5-10	$1.07\,10^{-7}$	$1.37\,10^{-4}$	$8.05\,10^{-3}$	$6.11\,10^{-1}$
Model B (1.2 keV)				
Energy (keV)	< 1.5 R$_*$	< 5 R$_*$	< 21 R$_*$	< 105 R$_*$
		MOS		
0.5-1.5	–	–	$2.09\,10^{-4}$	$1.44\,10^{-1}$
1.5-2.5	–	$5.37\,10^{-6}$	$1.61\,10^{-3}$	$4.48\,10^{-1}$
2.5-10	$7.22\,10^{-6}$	$3.07\,10^{-3}$	$5.51\,10^{-2}$	$2.67\,10^{-1}$
0.5-10	$7.26\,10^{-6}$	$3.08\,10^{-3}$	$5.70\,10^{-2}$	$8.85\,10^{-1}$
		pn		
0.5-1.5	–	–	$7.35\,10^{-4}$	$4.58\,10^{-1}$
1.5-2.5	–	$7.53\,10^{-6}$	$4.79\,10^{-3}$	$1.32\,10^{0}$
2.5-10	$4.25\,10^{-5}$	$1.20\,10^{-2}$	$1.53\,10^{-1}$	$6.90\,10^{-1}$
0.5-10	$4.25\,10^{-5}$	$1.20\,10^{-2}$	$1.59\,10^{-1}$	$2.48\,10^{0}$
		EPIC		
0.5-1.5	–	–	$3.33\,10^{-4}$	$2.18\,10^{-1}$
1.5-2.5	–	$5.88\,10^{-6}$	$2.36\,10^{-3}$	$6.54\,10^{-1}$
2.5-10	$1.55\,10^{-5}$	$5.17\,10^{-3}$	$7.81\,10^{-2}$	$3.67\,10^{-1}$
0.5-10	$1.55\,10^{-5}$	$5.18\,10^{-3}$	$8.09\,10^{-2}$	$1.26\,10^{0}$
Model C (WR 25)				
Energy (keV)	< 1.5 R$_*$	< 5 R$_*$	< 21 R$_*$	< 105 R$_*$
		MOS		
0.5-1.5	–	–	$4.16\,10^{-5}$	$1.54\,10^{-2}$
1.5-2.5	–	$2.53\,10^{-6}$	$2.43\,10^{-4}$	$4.71\,10^{-2}$
2.5-10	$8.29\,10^{-6}$	$1.70\,10^{-3}$	$1.66\,10^{-2}$	$5.92\,10^{-2}$
0.5-10	$8.40\,10^{-6}$	$1.71\,10^{-3}$	$1.69\,10^{-2}$	$1.24\,10^{-1}$
		pn		
0.5-1.5	–	–	$1.31\,10^{-4}$	$4.95\,10^{-2}$
1.5-2.5	–	$2.73\,10^{-6}$	$7.17\,10^{-4}$	$1.36\,10^{-1}$
2.5-10	$5.85\,10^{-5}$	$7.58\,10^{-3}$	$5.25\,10^{-2}$	$1.62\,10^{-1}$
0.5-10	$5.85\,10^{-5}$	$7.59\,10^{-3}$	$5.34\,10^{-2}$	$3.49\,10^{-1}$
		EPIC		
0.5-1.5	–	–	$6.26\,10^{-5}$	$2.34\,10^{-2}$
1.5-2.5	–	$2.58\,10^{-6}$	$3.55\,10^{-4}$	$6.80\,10^{-2}$
2.5-10	$2.01\,10^{-5}$	$3.08\,10^{-3}$	$2.50\,10^{-2}$	$8.34\,10^{-2}$
0.5-10	$2.02\,10^{-5}$	$3.09\,10^{-3}$	$2.55\,10^{-2}$	$1.77\,10^{-1}$

For each model and each position in the wind, we estimated the corresponding count rates. These are reported in Table 3.

If we stick to these norms, it is evident that model A plasma would not be detected by *XMM-Newton* if it is located below 5 R_* and will be detected as a rather hard source if it is just below 21 R_*. If located just below 105 R_*, a clear detection should be possible in all bands. Any cooler plasma has no chance of being more efficiently detected. Model B plasma located below 1.5 R_* will not be detected whereas it will only be detected in the hard band if put just below 5 R_*, in good agreement with Figs. 5 and 6. The case is very similar if the plasma is located just below 21 R_*, but a detection could still be possible in the medium band where one thousandth of the intrinsic flux is emerging. The model C plasma, which is certainly to be considered as an extreme case (owing to the high X-ray luminosity of WR 25), will be detected basically in the hard band even if it is situated slightly below 5 R_*. The pn detector could only reveal such a plasma in the medium band if it is located above 21 R_*. From Table 3, it is clear that the emerging flux for any plasma situated below 21 R_* will in any case be very hard. Some flux in the medium and soft bands could only be significantly present if one allows the emitting plasma to exist up to several tens of stellar radii.

5.3. Discussion of the results

Without a detection or a clear idea of the intrinsic spectrum of WR 40, it is difficult to transform the upper limits on the count rates (see Table 1) into upper limits on the flux. If we make the reasonable assumption that any possible X-ray emission coming out of WR 40 could be well represented by one of the combinations of the three models A, B, C and of the four positions of the plasma in the wind, we should be able to derive a viable upper limit on the flux. We computed, for each possibility, the maximum EM compatible with the corresponding upper limits on the count rates (for the 5×5 case), as well as the relevant fluxes. The resulting upper limits on the fluxes are contained in Table 4 for each instrument as well as for their combination. As expected, the most restrictive upper limits on the fluxes are constrained by the combined EPIC detector, this is a direct consequence of poissonian statistics. Having no information to select among the different models, we are obliged to adopt the less restrictive constraint. The largest upper limit is to be found for model C when situated below 1.5 R_*. We find $f_X(0.5-10\,\mathrm{keV}) = 4.66\,10^{-14}$ erg cm^{-2} s^{-1} and $f_X(2.5-10\,\mathrm{keV}) = 3.63\,10^{-14}$ erg cm^{-2} s^{-1}. The necessary total norms to reach these two flux values are 0.32 and 0.25 cm^{-5}, respectively. Therefore, the model will more easily be detected in the hard band (lowest norm and thereby EM). Recomputing the flux, in the total band, for a norm of 0.25 cm^{-5}, leads to the expected result of $f_X(0.5-10\,\mathrm{keV}) = 3.63\,10^{-14}$ erg cm^{-2} s^{-1} (since all the flux is located in the hard band). This

Table 4. Maximum observed flux reaching the Earth for our models of WR 40 and remaining compatible with the individual maximum observed count rates as estimated from our *XMM-Newton* observation (Table 1, the 5 × 5 case). These values are computed for each detector, for each model of emitting plasma and for each location in the wind of this plasma. The fluxes are given in erg cm^{-2} s^{-1}.

Model A (0.6 keV)									
Energy (keV)	< 1.5 R_*	< 5 R_*	< 21 R_*	< 105 R_*	Energy (keV)	< 1.5 R_*	< 5 R_*	< 21 R_*	< 105 R_*
		MOS1					pn		
0.5-1.5	–	–	$7.29\,10^{-18}$	$4.23\,10^{-15}$	0.5-1.5	–	–	$3.01\,10^{-18}$	$2.32\,10^{-15}$
1.5-2.5	–	$1.29\,10^{-19}$	$8.07\,10^{-15}$	$6.33\,10^{-15}$	1.5-2.5	–	$1.25\,10^{-19}$	$5.21\,10^{-15}$	$3.96\,10^{-15}$
2.5-10	$6.57\,10^{-14}$	$2.59\,10^{-14}$	$1.43\,10^{-14}$	$1.22\,10^{-14}$	2.5-10	$3.26\,10^{-14}$	$2.06\,10^{-14}$	$1.43\,10^{-14}$	$1.20\,10^{-14}$
0.5-10	$9.16\,10^{-14}$	$3.61\,10^{-14}$	$1.91\,10^{-14}$	$8.97\,10^{-15}$	0.5-10	$3.93\,10^{-14}$	$2.47\,10^{-14}$	$1.63\,10^{-14}$	$6.74\,10^{-15}$
		MOS2					EPIC		
0.5-1.5	–	–	$7.65\,10^{-18}$	$4.44\,10^{-15}$	0.5-1.5	–	–	$2.42\,10^{-18}$	$1.63\,10^{-15}$
1.5-2.5	–	$1.19\,10^{-19}$	$7.42\,10^{-15}$	$5.82\,10^{-15}$	1.5-2.5	–	$6.06\,10^{-20}$	$3.20\,10^{-15}$	$2.47\,10^{-15}$
2.5-10	$8.07\,10^{-14}$	$3.19\,10^{-14}$	$1.76\,10^{-14}$	$1.49\,10^{-14}$	2.5-10	$2.51\,10^{-14}$	$1.28\,10^{-14}$	$7.86\,10^{-15}$	$6.66\,10^{-15}$
0.5-10	$1.01\,10^{-13}$	$3.98\,10^{-14}$	$2.11\,10^{-14}$	$9.90\,10^{-15}$	0.5-10	$3.23\,10^{-14}$	$1.65\,10^{-14}$	$9.66\,10^{-15}$	$4.28\,10^{-15}$
Model B (1.2 keV)									
Energy (keV)	< 1.5 R_*	< 5 R_*	< 21 R_*	< 105 R_*	Energy (keV)	< 1.5 R_*	< 5 R_*	< 21 R_*	< 105 R_*
		MOS1					pn		
0.5-1.5	–	–	$1.93\,10^{-18}$	$4.25\,10^{-15}$	0.5-1.5	–	–	$9.35\,10^{-19}$	$2.27\,10^{-15}$
1.5-2.5	–	$2.10\,10^{-20}$	$7.37\,10^{-15}$	$6.69\,10^{-15}$	1.5-2.5	–	$2.80\,10^{-20}$	$4.64\,10^{-15}$	$4.24\,10^{-15}$
2.5-10	$8.86\,10^{-14}$	$4.04\,10^{-14}$	$1.94\,10^{-14}$	$1.42\,10^{-14}$	2.5-10	$3.79\,10^{-14}$	$2.61\,10^{-14}$	$1.76\,10^{-14}$	$1.38\,10^{-14}$
0.5-10	$1.23\,10^{-13}$	$5.63\,10^{-14}$	$2.65\,10^{-14}$	$1.22\,10^{-14}$	0.5-10	$4.57\,10^{-14}$	$3.14\,10^{-14}$	$2.07\,10^{-14}$	$9.46\,10^{-15}$
		MOS2					EPIC		
0.5-1.5	–	–	$2.03\,10^{-18}$	$4.46\,10^{-15}$	0.5-1.5	–	–	$6.98\,10^{-19}$	$1.61\,10^{-15}$
1.5-2.5	–	$1.94\,10^{-20}$	$6.78\,10^{-15}$	$6.15\,10^{-15}$	1.5-2.5	–	$1.10\,10^{-20}$	$2.89\,10^{-15}$	$2.63\,10^{-15}$
2.5-10	$1.09\,10^{-13}$	$4.97\,10^{-14}$	$2.38\,10^{-14}$	$1.74\,10^{-14}$	2.5-10	$3.08\,10^{-14}$	$1.79\,10^{-14}$	$1.02\,10^{-14}$	$7.72\,10^{-15}$
0.5-10	$1.36\,10^{-13}$	$6.22\,10^{-14}$	$2.92\,10^{-14}$	$1.35\,10^{-14}$	0.5-10	$3.97\,10^{-14}$	$2.31\,10^{-14}$	$1.29\,10^{-14}$	$5.92\,10^{-15}$
Model C (WR 25)									
Energy (keV)	< 1.5 R_*	< 5 R_*	< 21 R_*	< 105 R_*	Energy (keV)	< 1.5 R_*	< 5 R_*	< 21 R_*	< 105 R_*
		MOS1					pn		
0.5-1.5	–	–	$4.70\,10^{-19}$	$3.78\,10^{-15}$	0.5-1.5	–	–	$2.54\,10^{-19}$	$2.00\,10^{-15}$
1.5-2.5	–	$5.66\,10^{-21}$	$6.11\,10^{-15}$	$6.82\,10^{-15}$	1.5-2.5	–	$9.79\,10^{-21}$	$3.88\,10^{-15}$	$4.41\,10^{-15}$
2.5-10	$1.18\,10^{-13}$	$5.68\,10^{-14}$	$2.77\,10^{-14}$	$1.82\,10^{-14}$	2.5-10	$4.22\,10^{-14}$	$3.20\,10^{-14}$	$2.21\,10^{-14}$	$1.66\,10^{-14}$
0.5-10	$1.63\,10^{-13}$	$7.92\,10^{-14}$	$3.83\,10^{-14}$	$1.68\,10^{-14}$	0.5-10	$5.09\,10^{-14}$	$3.86\,10^{-14}$	$2.63\,10^{-14}$	$1.30\,10^{-14}$
		MOS2					EPIC		
0.5-1.5	–	–	$4.94\,10^{-19}$	$3.97\,10^{-15}$	0.5-1.5	–	–	$1.81\,10^{-19}$	$1.44\,10^{-15}$
1.5-2.5	–	$5.21\,10^{-21}$	$5.62\,10^{-15}$	$6.28\,10^{-15}$	1.5-2.5	–	$3.19\,10^{-21}$	$2.41\,10^{-15}$	$2.71\,10^{-15}$
2.5-10	$1.45\,10^{-13}$	$6.98\,10^{-14}$	$3.41\,10^{-14}$	$2.23\,10^{-14}$	2.5-10	$3.63\,10^{-14}$	$2.34\,10^{-14}$	$1.37\,10^{-14}$	$9.61\,10^{-15}$
0.5-10	$1.80\,10^{-13}$	$8.75\,10^{-14}$	$4.22\,10^{-14}$	$1.85\,10^{-14}$	0.5-10	$4.66\,10^{-14}$	$3.00\,10^{-14}$	$1.74\,10^{-14}$	$8.09\,10^{-15}$

hard flux is little influenced by the ISM and we translate it to an ISM corrected upper limit of $f_X^{unabs}(0.5-10\,keV) = 3.7\,10^{-14}$ erg cm^{-2} s^{-1}. If we adopt for WR 40 a distance of 3 kpc and a bolometric luminosity of $4\,10^5$ $L_\odot$ (taken from the work of Herald et al. 2001), this upper limit on the flux corresponds to an upper limit on the X-ray luminosity $L_X(0.5–10\,keV) = 4\,10^{31}$ erg s^{-1} and the luminosity ratio $L_X/L_{bol} = 2.6\,10^{-8}$. This upper limit is very conservative. A more restrictive upper limit could possibly be derived if, for example, one made the assumption that the emitting plasma persists well above 21 R_* up to 105 R_*. This upper limit on the flux is then given by $f'_X(0.5-10\,keV) = 8.09\,10^{-15}$ erg cm^{-2} s^{-1} (again model C) and is rather soft. It translates into an ISM corrected upper limit $f_X^{unabs}(0.5-10\,keV) = 8.6\,10^{-15}$ erg cm^{-2} s^{-1}, $L_X(0.5–10\,keV) = 9.2\,10^{30}$ erg s^{-1} and

$L_X/L_{bol} = 6.0\,10^{-9}$. This second more severe albeit less universal limit is subordinated to an a priori knowledge on the 'observed' X-ray spectral distribution of the source.

The X-ray luminosity of bright High-Mass X-ray Binaries (HMXBs) is typically in the range $L_X(2 - 10\,\mathrm{keV}) = 10^{37}$–$10^{38}$ erg s^{-1} (Grimm et al. 2002, Sasaki et al. 2003). These stars correspond to supergiants with compact companions. Skinner et al. (2002a) also find $L_X \sim 10^{37}$ erg s^{-1} in the hypothetical case of an accreting compact companion for the WR star WR 110. These figures are six orders of magnitude larger than the upper limit set on WR 40. Due to its strength and its hardness, such an X-ray emission would have been detected even if buried down to 1.5 R_* in the wind of WR 40. This represents a strong argument against the presence of an accreting compact companion around WR 40. Some physical process would be needed to inhibit the accretion or at least the X-ray emission associated with it (see e.g. Stella et al. 1986). Although the WR + compact companion stage is consistent with some evolutionary scenari of massive binaries (van den Heuvel 1976), no such object has been securely identified up to now, except perhaps Cygnus X-3 (see also Tutukov & Cherepashchuk 2003). For years, another good candidate for harbouring a compact companion has been the WR star WR 6. Recently, Skinner et al. (2002b) have rejected the compact companion hypothesis on the basis of the observed luminosity of the X-ray emission of WR 6. They tentatively explain the X-ray emission (essentially the hot component) as due to the wind of the WR star impacting on a low-mass non-degenerate companion.

Other WN stars have been observed recently in the X-ray domain. The X-ray brightest WN star WR 25 (Raassen et al. 2003) is supposed to emit hard radiation due to a collision phenomenon between the WR wind and the wind of a putative companion. We have shown that a radiation similar to the one of WR 25 would have been detected even through the wind of WR 40. WR 110 was observed by Skinner et al. (2002a) because it was reputed single. However, in the X-ray domain, the star exhibits a strong X-ray emission even including a hard component. These authors finally conclude that WR 110 is most probably a colliding wind binary star. In the paper on WR 6, they further underline the strong similarities between both stars: the X-ray spectra and luminosities of WR 6 and WR 110 are indeed very similar ($L_X(0.2 - 10\,\mathrm{keV}) \sim 4$–$5\,10^{32}$ erg s^{-1}). This luminosity is still more than one order of magnitude stronger than the conservative limit on WR 40. The discrepancy is larger when compared to the second limit of $L_X(0.5$–$10\,\mathrm{keV}) = 9.2\,10^{30}$ erg s^{-1}. The latter might apply here since the possible wind-wind collision region is not necessarily buried deep in the WR wind (except perhaps in the case of a WR + WR binary), depending e.g. on the system separation. As a conclusion, it is clear that WR 40 is not at all comparable to the class of objects that are considered nowadays as representative of WR + O colliding wind binaries. It should however be noted that the origin, in this class, of the hot component as being in the shock zone is still a working hypothesis.

Markedly puzzling in this respect is the observation of WR 1 (WN4) by Ignace et al. (2003) who suspect that the hot component is absent in WR 1; they further argue that it could be the first example of an X-ray emission generated by a single WR star: a soft intrinsic emission due to shocks resulting from hydrodynamical instabilities in the wind. However, the observed count rates for WR 1 are still a factor 100 larger than our secure limit on WR 40.

Our observation of the WN8 star WR 40 demonstrates that there exist some WR stars (probably single) that are not significantly emitting X-ray photons (at least within the sensitivity limit of present detectors). If we join this result with the conclusion of Oskinova et al. (2003) stating that there is no detected X-ray emission from a single WC star, we may wonder whether single WR stars are able to emit X-ray radiation.

Similar to OB stars, WRs are known to exhibit intrinsically unstable winds. The current picture of the X-ray emission from O stars is that a soft emission is produced by a plasma heated in shocks due to hydrodynamical instabilities present in the line-driven winds. Runacres & Owocki (2002) have shown that the clumpiness of O star winds may propagate far out into the wind but the abrupt velocity discontinuities that are supposed to generate the hot emitting plasma are much rarer and much weaker beyond a distance from the star of roughly a few tens of stellar radii. The high temperature regions are much less hot and much less frequent. Assuming that instabilities of WR winds (see Gayley & Owocki 1995) also produce a similar X-ray emission, we have shown here or at least confirmed that soft X-rays emitted below some 5 R_* in WR 40 have no chance to escape and that those emitted below 20 R_* have very little chance to escape. We showed that, even if a significant X-ray radiation appears in the wind, the emergent X-ray emission might be quite low essentially due to the optical depth of the wind. Therefore, we agree with Oskinova et al. (2003) and extend their conclusion by suggesting that there exists a population of WR stars (WC *and* WN) that are not significantly emitting X-rays. The deep reason is probably the very large optical depth of the envelope and the relatively deep position of any potential X-ray source intrinsic to the wind. It is possible that other WN stars, apparently very similar, but either with a less dense or with an anisotropic or inhomogeneous wind may allow some leakage. It is clear that a marked clumpiness or a fragmentation of the wind may be determinant to change the situation. These effects have been invoked in the case of O stars (Kramer et al. 2003, Feldmeier et al. 2003).

The case of WR 1 is very interesting. Indeed, with a mass-loss rate of $\dot{M} = 10^{-4.838}$ M$_\odot$ yr^{-1} (6.9 times lower than for WR 40) and a terminal velocity of $v_\infty = 1600$ km s^{-1} (1.9 times larger, see Ignace et al. 2003), the ratio $\dot{M}/v_\infty$ (which is part of the expression of the density of the wind) is 13 times lower than for WR 40. However, the two stars have much different radii (about a factor of five in favour of WR 40) and this difference strongly attenuates the impact of the above-mentioned ratio on the resulting

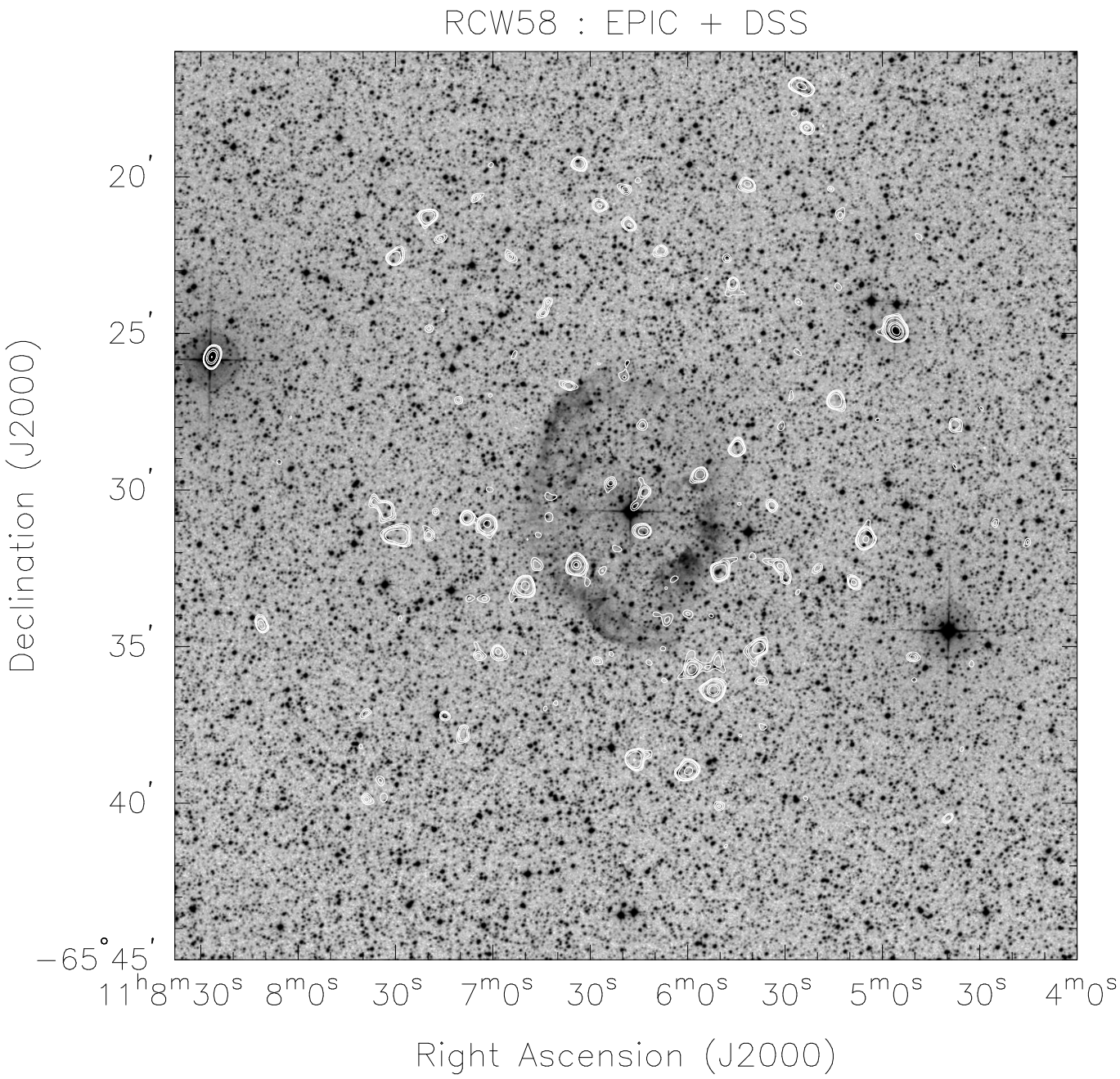

Fig. 7. DSS view in the R filter including the field observed with *XMM-Newton*. WR 40 is the central object. We superposed contours from the smoothed combined X-ray image with contour levels at values of 0.55, 0.6, 0.65, 0.8, 1.5, 2.0 and 3.0 counts per pixel^2. The nebula RCW 58 surrounding WR 40 is particularly visible in the Hα line but no X-ray radiation can be associated to it. The bright star at the W-SW not detected as an X-ray source is HD 96265 (M0III).

optical depth. However, the earlier spectral type of WR 1 suggests a higher ionization. Therefore, the wind of WR 1 may be comparatively slightly more transparent to X-rays: this could explain its detection. Only detailed modelling beyond the scope of the present paper will answer this question.

6. The surrounding nebula RCW 58

Figure 7 exhibits an R plate of the Digitized Sky Survey with the X-ray contours based on the smoothed version of the combined X-ray image superimposed on it. The contour levels have been chosen to underline weak fluctuations. As will be shown below, the *XMM-Newton* astrometry is accurate enough for the superposition to be meaningful. Incidentally, before discussing the nebula, we draw the attention of the reader to the region of WR 40 again. The weak background fluctuation is particularly visible on this figure as well as its decentred nature with respect to WR 40. This further illustrates our conclusions on the non-detection of this object.

Clearly a few sources are visible in the field. We performed a systematic search for point-like sources that will be described in Sect. 7. In the present section, we will focus on the case of the diffuse sources.

WR 40 is surrounded by an ejecta nebula named RCW 58. Its dynamics have been studied by Smith et al. (1984, 1988). It consists of a shell expanding from the central star WR 40 and enveloping slower moving clumps of stellar ejecta from a previous evolutionary stage. The optical image is particularly suitable to show the structure of the nebula. Dedicated pictures in the Hα and the [O III] lines can be found in the study of Gruendl et al. (2000, their figure 3). From an inspection of the latter and of our Fig. 7, it is clear that there exists no systematic possibility to associate either a diffuse X-ray emission (or background fluctuation) or a set of individual sources with the genuine nebula. The nebula is not emitting any discernible X-ray radiation.

From this absence of detection of RCW 58 in the X-ray domain, we may derive an upper limit on its X-ray luminosity. The expected source of X-rays being most probably diffuse and extended, we cannot treat the present case in the same way as the WR 40 case in Sect. 4. The size of RCW 58 as compared to the field of view of *XMM-Newton* renders the problem intricate because it turns out to be very difficult to estimate the background independent of the estimation of the counts due to the nebula itself. We will adopt a very conservative approach by attributing the whole background to the nebula. Although nothing is detected in any band, the possible nebular X-ray emission should be primarily soft. In the soft band, we observe, for the 5 by 5 pixel basic area, 0.9 counts in MOS1, 1.1 counts in MOS2 and 1.1 counts in pn (see Table 1). These values correspond to $2.4\,10^{-3}$ counts s^{-1} arcmin^{-2} for the combined MOS detector and $2.1\,10^{-3}$ counts s^{-1} arcmin^{-2} for the pn one. These values are in perfect agreement with the respective values $2.0\,10^{-3}$ counts s^{-1} arcmin^{-2} and $2.1\,10^{-3}$ counts s^{-1} arcmin^{-2} given in the *XMM-Newton* users' manual for the quiescent background. The agreement is also good with the results of the detailed study of the pn background by Katayama et al. (2004). The latter present evidence for persistent fluctuations of the quiescent background amounting to 8 per cent (1σ). Admitting a 3σ limit, up to 24 per cent of the expected mean background might be absent. This means that most of the counts can be attributed to the background and that one quarter of the conservative upper limit would still be a reasonable border. Adopting this more restrictive limit, we implicitly make the hypothesis that these background studies fully apply to our case. Indeed, we prefer to adopt the conservative limit, keeping in mind that a more restrictive one is available under certain conditions. The shape of the nebula in the optical can be well approximated by an ellipse with main axis dimensions of $9'$ by $6\farcm5$ (see Marston et al. 1994, Chu 1988). Assuming that the X-ray emission fills up the total surface of the nebula in a uniform way ($9'$ by $6\farcm5$ gives 45.9 arcmin^2), we derive count rates for the total nebula of 0.049 counts s^{-1} for MOS1, 0.059 counts s^{-1} for MOS2 and 0.097 counts s^{-1} for pn. Poisson errors translated on these count rates do not exceed 4 per cent. To convert these count rates into fluxes, we need a model for the X-ray emitting plasma. Absorbed MEKAL models have been proven adequate for fitting the X-ray emission of the two detected WR bubbles NGC 6888 and S 308. A temperature corresponding to 0.24 keV has been associated to NGC 6888 (Gruendl et al. 2003) whereas $kT = 0.10$ keV has been deduced for S 308 (Chu et al. 2003b). Using the above mentioned count rates related to the adopted conservative limit, the same interstellar column as for WR 40, and the MEKAL models quoted above, we derive $3.06\,10^{-13}$ erg cm^{-2} s^{-1} (MOS1), $3.70\,10^{-13}$ erg cm^{-2} s^{-1} (MOS2) and $1.41\,10^{-13}$ erg cm^{-2} s^{-1} (pn) as the fluxes corresponding to $kT = 0.24$ keV. For $kT = 0.10$ keV, we obtained fluxes of $4.10\,10^{-13}$ erg cm^{-2} s^{-1} (MOS1), $4.96\,10^{-13}$ erg cm^{-2} s^{-1} (MOS2) and $1.43\,10^{-13}$ erg cm^{-2} s^{-1} (pn). The most stringent constraint comes from the pn detector, which is not surprising. These fluxes convert into the unabsorbed fluxes $f_{\rm X}^{\rm unabs}(0.5-1.5\,{\rm keV}) = 5.3\,10^{-13}$ erg cm^{-2} s^{-1} for $kT = 0.24$ keV and $f_{\rm X}^{\rm unabs}(0.5-1.5\,{\rm keV}) = 1.1\,10^{-12}$ erg cm^{-2} s^{-1} for $kT = 0.10$ keV, corresponding to luminosities at 3 kpc $L_{\rm X}(0.5-1.5\,{\rm keV}) = 5.7\,10^{32}$ erg s^{-1} ($\log L_{\rm X} = 32.76$) and $L_{\rm X}(0.5-1.5\,{\rm keV}) = 1.2\,10^{33}$ erg s^{-1} ($\log L_{\rm X} = 33.07$), respectively.

These values can be compared to the predictions of the so-called 'standard' model of bubbles. In particular, García-Segura & MacLow (1995) have presented the formalism for evaluating the X-ray luminosity of an ellipsoidal bubble blown by a WR. García-Segura & MacLow (1995) introduced ellipsoidality in their models directly inspired by the observational results but gave no clue of its physical origin. Using this formalism, the prediction relies on four observables: the expansion velocity (87 km s^{-1} according to Smith et al. 1988, 110 km s^{-1} according to Chu 1988), the total mass of the nebula (3.2 $M_\odot$, value deduced from Smith & Batchelor 1970, after conversion for a distance of 3 kpc) and the sizes of the major and minor axes of the ellipse (3.9 pc by 2.8 pc again for a distance of 3 kpc). With these parameters, we predict minimum X-ray luminosities in the 0.5–1.5 keV range of $\log L_{\rm X} = 33.8$ ($kT = 0.24$ keV) or of $\log L_{\rm X} = 32.8$ ($kT = 0.10$ keV). These values are close to the very conservative upper limits derived from the observations. In particular, we can conclude that, for the hottest plasma, the predictions of the García-Segura & MacLow model are certainly too large by at least a factor 5. Without detection, it is always possible of course to invoke a cooler plasma to solve the problem but one should also keep in mind that the limits decreased by a factor of 4 are still quite reasonable. In this particular case, even the cool plasma model is rejected.

Numerical simulations specific to the case of RCW 58 were performed by Arthur et al. (1996) and Freyer et al. (2003). Arthur et al. (1996) predicted the X-ray luminosity of the bubble as a function of the mass-loading phenomenon and of the age of the structure, but without tak-

ing into account the mass-loss history of the star. For an age larger than 10^4 years (as deduced from the dynamical time-scale of the nebula), the logarithmic X-ray luminosity is about 32.5 without mass loading and, in any case, larger than 33 with mass loading. However, Arthur et al. (1996) adopted an energy range of 0.16-3.5 keV and a distance to the object of 2 kpc. Using these parameters with a mean temperature $kT = 0.3$ keV, as appropriate for their model, we then derive a new upper limit corresponding to our *XMM-Newton* data of $\log L_X = 32.6$. Our observations thus clearly rule out the mass-loaded case of Arthur et al. (1996). This seems strange since the nebula presents a very clumpy morphology that supports the idea of the importance of mass loading. From recent simulations of RCW 58, Freyer et al. (2003) predicted a logarithmic X-ray luminosity of 33.8 in the range 0.5-3.0 keV. Again, the model X-ray emission exceeds our upper limit.

Although many galactic WR stars possess a wind-blown bubble and theory suggests that shocked, hot gas should be present inside these bubbles (Weaver et al. 1977), only two of them are known to be X-ray emitters up to now. NGC 6888 around WR 136 (WN6) is often regarded as the archetypal WR bubble. It was first detected in the X-ray domain by the *EINSTEIN* satellite, but was more thoroughly studied using *ROSAT* data (Wrigge et al. 1994 and references therein). The X-ray emission from NGC 6888 appears to be limb-brightened and is concentrated to the northeast and southwest parts of the nebula, where Hα appears the strongest. Due to the morphology of the nebular Hα and [O III] emissions, García-Segura & MacLow (1995) and Gruendl et al. (2000) have suggested that the progenitor of WR 136 was a Red Supergiant (RSG) and that the dense wind ejected during this phase is presently in collision with the fast WR wind. García-Segura & MacLow (1995) were able to predict the X-ray luminosity of NGC 6888 on the basis of the observed properties of the nebula. This evaluation is rather close to the *ROSAT* luminosity $\log L_X = 34.2$. The second example of an X-ray emitting bubble is S 308 (around WR 6, WN4) that was discovered with the *ROSAT* satellite, and the nebula was recently reobserved with the *XMM-Newton* facility (Chu et al. 2003b and references therein). S 308 appears to share many properties with NGC 6888: the nebula is also limb-brightened in the X-ray domain and its morphology in the nebular lines also suggests an RSG progenitor for the central star. The WR bubble is apparently still embedded in the wind ejected during the RSG phase of the star. However, it will soon reach the limit of this wind since a breakout already exists to the northwest of the shell (Chu et al. 2003a).

On the other hand, three WR bubbles were not detected in X-rays: NGC 2359, NGC 3199 (Chu et al. 2003a, *ROSAT*) and RCW 58 (present work, *XMM-Newton*). The first two have rather low expansion velocities (around 20 km s^{-1}). The total absence of X-ray emission for RCW 58 is much more puzzling. The predictions of the standard model are rather close to the conservative observational limits we adopted but no hint of weak emission is suspected. In addition, from the cases of NGC 6888 and S 308, we expect the X-ray emission to be non-uniform, but concentrated on the limb. Therefore, we should have detected these limbs in our observation. Indeed, if the same luminosity was distributed over a fraction $1/m$ of the total surface, the corresponding observed count rates per unit of solid angle relevant to this smaller surface would be multiplied by m and would thus be much easier to detect. Therefore, one could envisage to put a tighter constraint by adopting a model for the limb brightening. However, we think there is little sense in doing that. Indeed, since RCW 58 is not detected, the limb brightening model has to be derived from observed limb brightening from other objects such as NGC 6888 and/or S 308 which would assume a strong similarity between RCW 58 and these nebulae (an unfounded hypothesis actually). The other possibility would be to rely on pure models. But one may wonder why to rely on such models for limb brightening characteristics while they are unable to reproduce the right global luminosity.

The more realistic models of Arthur et al. (1996) with mass loading and of Freyer et al. (2003), not only predict such a limb brightening, but also estimate an intense X-ray emission which is clearly not observed here. The main differences between RCW 58 and NGC 6888 and/or S 308 are linked to the nature of the progenitor as deduced from the nebula morphology. Indeed, the clear presence of clumps in the nebula could indicate that the WR wind has reached the material from a previous ejection (a possible Luminous Blue Variable phase, LBV). However, the past existence of an LBV phase for WR 40 is not supported by other aspects like e.g. the chemical abundances of the nebula (see Smith 1996 for a discussion). The separation between the Hα shell and the [O III] one (see e.g. Gruendl et al. 2000) is probably an indication: we may imagine that the hot gas begins to overtake the shell and to dilute itself into the low density interior of the main-sequence shell, preventing its detection in the X-ray domain. We may also imagine that a peculiar property of the LBV phase renders the shocked gas undetectable with *XMM-Newton*. This remains extremely speculative. For the moment, the only sound conclusion is that the absence of detection of X-ray emission in RCW 58 is most probably related to the particular morphology of this nebula. Further X-ray studies of WR bubbles (including M1-67) will be necessary before a clear scheme can emerge.

Finally, searching for other diffuse X-ray emission, a look at Fig. 7 tells us that the only strange feature that could be an actual diffuse emission is some kind of banana like structure at α(J2000) = $11^h\ 05^m\ 40^s$ δ(J2000) = $-65°\ 32'\ 15''$ (around sources #13, #7 and #8, see Sect. 7.1). Further observations will be necessary to confirm the actual existence of this diffuse X-ray emission.

7. Search for X-ray sources in the field

The pointing to WR 40 reveals several X-ray sources, most of them being previously unknown. The combined EPIC image covers a circular field around WR 40 with a radius of about 15 arcmin. It is reproduced in Fig. 3, where several bright and many faint discrete sources can easily be spotted. In the following, we establish a catalog of these X-ray sources.

7.1. Detection

In order to produce the catalog of these serendipitous sources as displayed in Table 5, we used the source detection algorithms implemented in the SAS version 5.3.3 together with visual checks, according to the following steps:

- We ran the task EBOXDETECT first in local detection mode and, after estimating the background map with ESPLINEMAP, ran it again in map detection mode on the set of 9 images corresponding to the 3 different detectors (pn, MOS1 and MOS2) and the three energy bands defined in Section 3. A minimum total logarithmic likelihood of 12 was chosen, as it is the highest value for which at least all the sources visible by eye on the EPIC image are selected by the algorithm.
- The task EMLDETECT applied on the list resulting from the EBOXDETECT task with a minimum logarithmic likelihood of 12 (corrected value[1]: 3.78) provided a set of 38 sources. We also ran the EMLDETECT task on three individual evident sources which were not detected in all three instruments: source #6 is bright but only detected in the field of the pn; source #33 is also bright but only appears in the field of the MOS2; finally, source #10 is clearly seen on the MOS1 and MOS2 but falls in a gap between the pn CCDs. This makes a total of 41 sources at this stage.
- After performing a visual check to reject spurious detections or very faint sources only visible in one detector, we were left with the 33 high-grade X-ray sources listed in Table 5.

Besides the internal numbering, the source designation in Table 5 follows the naming conventions recommended by the *XMM* SOC and the IAU: the XMMU J prefix is followed by the right ascension HHMMSS.s (in hours, minutes, seconds and tenths of seconds, equinox J2000) and the declination of the source ±DDMMSS (in degrees, arcminutes, arcseconds, equinox J2000), both truncated, not rounded.

The count rates in the total energy band (i.e. 0.5–10 keV) are listed in Table 5 for each instrument when the relative error is smaller than 2. They are corrected for the background, for the contribution of the psf outside the detection box and for vignetting. For the extremely soft source #12, the counts are given in the soft band. Finally, the hardness ratios defined by

$$HR_1 = \frac{\text{Medium} - \text{Soft}}{\text{Medium} + \text{Soft}}$$

and

$$HR_2 = \frac{\text{Hard} - \text{Medium}}{\text{Hard} + \text{Medium}},$$

are given for the pn, provided the absolute error is ≤ 0.5.

Figure 8 gives the total EPIC X-ray image where the detected sources are marked by circles and labelled with their internal number.

The faintest detected sources have corrected count rates of about $2\,10^{-3}$ counts s^{-1} in pn and $1\,10^{-3}$ counts s^{-1} in MOS1 and MOS2. However, to set an upper limit on the WR40 count rates (the ones that were used in Sect. 4), it is necessary to compute the corresponding count rates that the faintest sources should have to be detected at the expected location of WR40, i.e. close to the centre. Correcting for the vignetting and exposure time ratios between the source locations and the WR40 expected position, we find upper limits of $1\,10^{-3}$ counts s^{-1} and $5\,10^{-4}$ counts s^{-1} in pn and MOS1/2 respectively. These values stand for the source search as performed simultaneously in the three EPIC detectors and in the three energy bands.

7.2. Optical and infrared counterparts

The positions of the 33 X-ray sources found in the present *XMM-Newton* observations have been cross-correlated with the Guide Star Catalogue (version 2.2)[2] and the All-Sky Data Release of the Two Micron all Sky Survey[3]. It was not possible to find an optimal cross-correlation radius from the fit of the relation proposed by Jeffries et al. (1997). The reason for this is that the distribution of the observed correlation radii is compatible with a random distribution of the X-ray sources in this highly crowded field. This is true for both the optical and the infrared catalogs. Based on the size of the FWHM of the *XMM-Newton* psf, we chose a maximum correlation radius of 5″. This conclusion should also be considered for the next steps in the identification process.

Table 5 lists all the unique candidate identifications within 5″ for the 33 EPIC sources. The following figures can be extracted:

- 18 EPIC sources have one optical counterpart.

[1] According to the XMM-NEWTON NEWS #29, the actual threshold in likelihood is more than two times lower than the one given by the LIKEMIN parameter. However, this has no direct influence on our results, since the sources have been preselected with EBOXDETECT and then visually checked.

[2] The Guide Star Catalogue-II is a joint project of the Space Telescope Science Institute and the Osservatorio Astronomico di Torino.

[3] 2MASS is a joint project of the University of Massachusetts and the Infrared Processing and Analysis Center/California Institute of Technology, funded by the National Aeronautics and Space Administration and the National Science Foundation.

Table 5. X-ray properties of 33 sources found in the field of WR40, with optical (GSC2.2 catalog) and infrared (2MASS catalog) counterparts for a matching radius $\leq 5''$. The count rates are given for the full energy range [0.5–10 keV], except for source #12 [0.5–1.5 keV]. The hardness ratios are given in pn except when stated otherwise and when the absolute error $\sigma \leq 0.5$. n is the number of counterparts within the adopted matching radius and d is the angular separation between the X-ray source and the counterpart when unique (see text for details).

#	XMMUJ	pn	MOS1	MOS2	HR_1	HR_2	GSC						2MASS				
							n	d ($''$)	name	B	V	R	n	d ($''$)	name	J	H	K
		10^{-3} cts/s	10^{-3} cts/s	10^{-3} cts/s														
1	110456.0-652454	37.8 ± 2.9	14.8 ± 1.4	12.5 ± 1.3	-0.75 ± 0.05	-0.05 ± 0.20	1	0.5	S1112310218	9.3	8.9		1	0.6	11045616-6524545	8.1	7.9	7.8
2	110504.9-653133	10.6 ± 1.4	4.0 ± 0.7	3.4 ± 0.6	0.13 ± 0.19	0.43 ± 0.12	0						0					
3	110508.8-653255	5.0 ± 1.1			-0.30 ± 0.21	0.16 ± 0.32	0						0					
4	110514.7-652706	8.7 ± 1.4		2.5 ± 0.6	0.18 ± 0.21	0.23 ± 0.16	0						0					
5	110524.0-651825	10.3 ± 9.5	2.9 ± 3.5	3.2 ± 1.3		0.85 ± 0.15	0						0					
6	110525.1-651706*	48.6 ± 4.4			-0.78 ± 0.05	-0.17 ± 0.32	1	1.3	S11123109541		15.6	14.6	2					
7	110529.7-653251	2.2 ± 0.8	0.9 ± 1.7		0.04 ± 0.47	0.19 ± 0.43	1	3.1	S11123102767		13.5	12.9	2					
8	110531.4-653227	3.1 ± 0.8	0.9 ± 0.4		-0.16 ± 0.41	0.58 ± 0.24	0						0					
9	110537.7-653502		1.5 ± 1.4	2.0 ± 0.5	-0.72 ± 0.28		1	1.6	S111202025544		15.7	15.2	1	1.6	11053759-6535008	13.3	12.6	12.4
10	110541.4-652012*		6.0 ± 1.2	6.0 ± 1.1	$-0.47 \pm 0.25^{\dagger}$	$0.65 \pm 0.18^{\dagger}$	0						0					
11	110544.8-652841	2.2 ± 0.7	3.9 ± 0.5	3.0 ± 0.5	0.47 ± 0.35	-0.11 ± 0.36	1	3.8	S11123104144		17.3	17.8	1	4.1	11054416-6528422	15.8	15.1	14.9
12	110546.2-652321*	2.5 ± 0.6	0.9 ± 0.4	0.8 ± 0.3			1	0.4	S11123106301			17.1	1	0.7	11054629-6523217	14.8	14.2	14.0
13	110550.1-653238	6.9 ± 1.0	1.4 ± 0.3	1.4 ± 0.4	-0.02 ± 0.19	0.39 ± 0.13	0						0					
14	110551.9-653624	15.8 ± 1.5	4.6 ± 0.6	5.3 ± 1.6	-0.66 ± 0.06	-0.09 ± 0.21	1	0.7	S111202024749		15.3	14.7	1	0.8	11055212-6536245	12.5	11.8	11.6
15	110555.9-652928	3.8 ± 0.8	1.2 ± 0.4	0.7 ± 0.3	-0.11 ± 0.37	0.60 ± 0.19	0						0					
16	110558.5-653545	3.3 ± 1.0	1.2 ± 0.4	1.3 ± 0.4		0.84 ± 0.41	0						0					
17	110559.6-653859	9.0 ± 1.6	4.9 ± 0.7	4.3 ± 0.6	-0.18 ± 0.17	-0.26 ± 0.29	0						0					
18	110613.4-653121	2.0 ± 1.0		1.3 ± 0.4	0.02 ± 0.50		1	4.4	S11123103245		17.3	16.4	2					
19	110616.5-653837	6.7 ± 1.3	3.2 ± 0.6	2.3 ± 0.6	-0.45 ± 0.19	0.14 ± 0.32	0						0					
20	110617.7-652134	2.9 ± 4.5	1.8 ± 0.7				1	2.4	S11123107135		14.7	15.0	1	2.5	11061801-6521356	13.1	12.7	12.6
21	110633.3-651934	9.8 ± 1.8	2.4 ± 2.6	4.4 ± 1.1	0.03 ± 0.21	0.23 ± 0.21	0						0					
22	110634.4-653223	10.0 ± 1.2	3.2 ± 0.5	2.5 ± 0.4	0.01 ± 0.15	0.28 ± 0.13	0						0					
23	110650.1-653302		4.6 ± 0.6	4.9 ± 0.6	$-0.02 \pm 0.14^{\dagger}$	$0.41 \pm 0.11^{\dagger}$	0						0					
24	110658.6-653508	3.1 ± 0.9		0.9 ± 1.5	-0.25 ± 0.34	0.37 ± 0.33	1	4.4	S111202025370		16.3	15.9	1	4.4	11065926-6535108	14.5	14.1	13.9
25	110701.8-653103	7.2 ± 1.0	2.0 ± 0.4	3.8 ± 0.5	-0.02 ± 0.17	0.32 ± 0.14	0						0					
26	110705.0-653518		0.7 ± 0.4	1.0 ± 0.5	-0.74 ± 0.21		1	2.8	S111202025317		17.6	16.3	1	2.1	11070502-6535164	14.5	13.8	13.5
27	110708.0-653050	4.4 ± 3.7		1.5 ± 0.4		0.40 ± 0.18	1	3.2	S111202027863		15.5	15.3	1	3.1	11070795-6530479	13.9	13.6	13.4
28	110719.5-652116	10.7 ± 1.9	3.2 ± 0.9	5.1 ± 1.1	-0.25 ± 0.14	-0.22 ± 0.33	1	1.9	S11123107225		16.3	15.1	2					
29	110728.5-653128	7.7 ± 1.2	2.3 ± 0.6		-0.14 ± 0.17	0.26 ± 0.18	1	3.2	S111202027512		17.4	17.2	1	2.9	11072830-6531258	15.4	14.9	14.8
30	110730.0-652235	11.5 ± 6.4	2.0 ± 0.8	4.1 ± 1.0	-0.81 ± 0.10		1	0.2	S11123106588		16.9	16.2	1	0.3	11073002-6522361	12.5	11.8	11.5
31	110731.9-653126		1.2 ± 0.4	1.6 ± 0.5	-0.59 ± 0.22		1	2.1	S111202027527		15.9	15.6	1	2.3	11073226-6531250	13.9	13.5	13.3
32	110811.6-653415	11.2 ± 2.1		3.4 ± 0.8	-0.88 ± 0.12		1	3.1	S111202025827		15.3	14.9	1	3.1	11081215-6534167	13.3	12.7	12.6
33	110826.1-652539*			40.2 ± 2.9	$-0.86 \pm 0.03^{\dagger}$	$-0.35 \pm 0.29^{\dagger}$	1	3.6	S1112310222	8.5	7.2		1	3.6	11082634-6525427	5.1	4.5	4.5

*: #6 only present in the field of view of the pn; #10 falls in a gap between the pn CCDs; #12: the reported rates come from the soft band; #33 only detected in the field of view of the MOS2.
†: *HR* measured with MOS2 instead of pn due to gap or field constraints.
remark: #1 is HD 96309; #33 is HD 96920

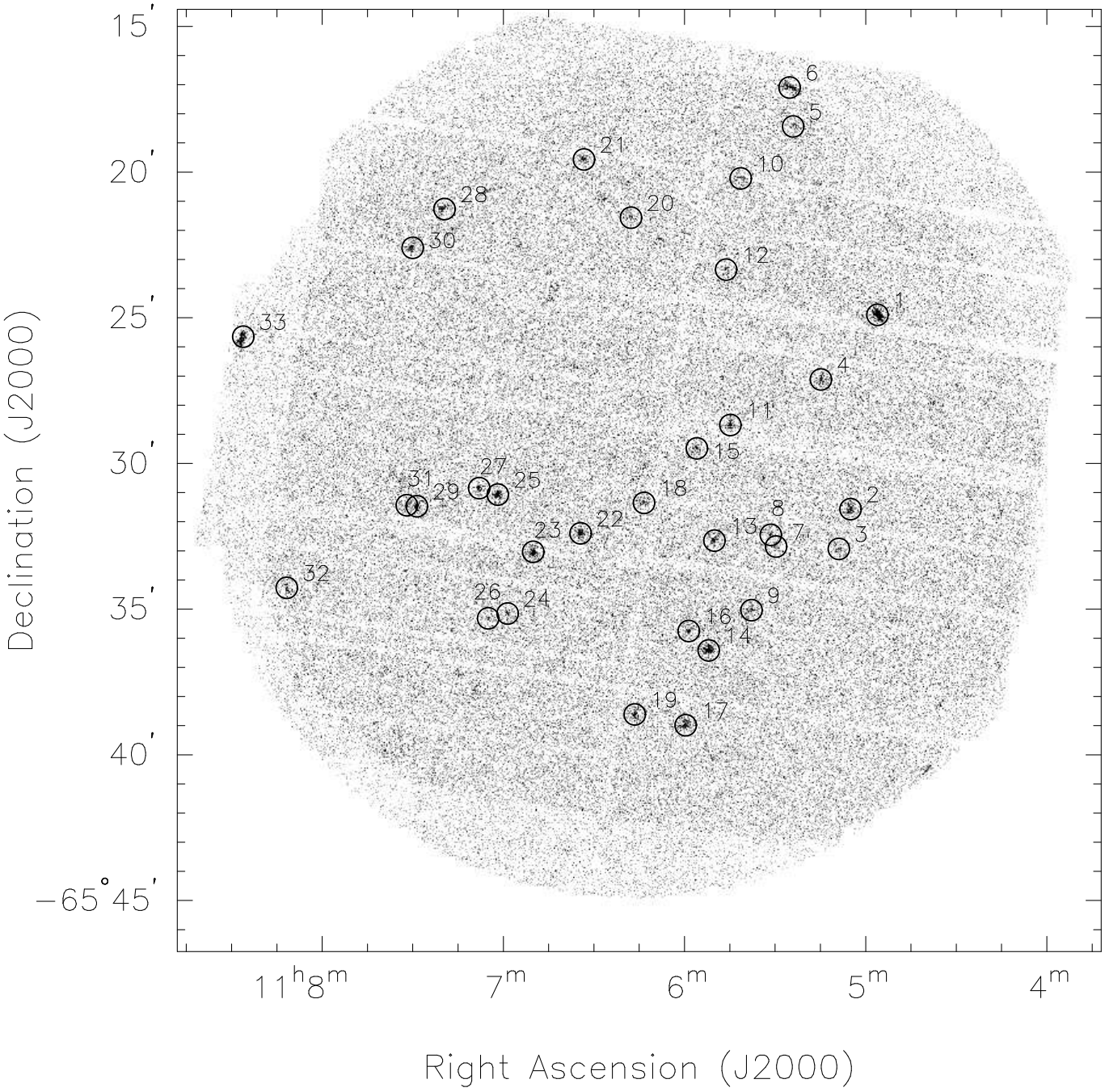

Fig. 8. Combined EPIC X-ray image of the field in the total energy band. The different point sources listed in the present catalog are labelled with their main entry in Table 5.

– all EPIC sources with an optical counterpart have at least one infrared counterpart at the same angular distance (4 have two infrared counterparts).
– 15 EPIC sources have no counterpart at all. They include the two objects with the hardest X-ray emission (#5 and #16).

Most of the sources are optically faint. Among the three brightest sources in X-ray, two are associated with stars having an HD number: #1 = HD 96309 (spectral type F2V, Houk & Cowley 1975) and #33 = HD 96920 (spectral type: G8III, Houk & Cowley 1975) which was also detected with ROSAT (= 1RXS J110825.5–652531).

7.3. X-ray properties

Figure 9 gives the respective distribution of the hardness ratios: a simple look suffices to be convinced that several sources are soft and several others are rather hard with little contribution in the intermediate regime.

It is interesting to remark that most of the sources with no optical counterpart (and thus no 2MASS counterpart)

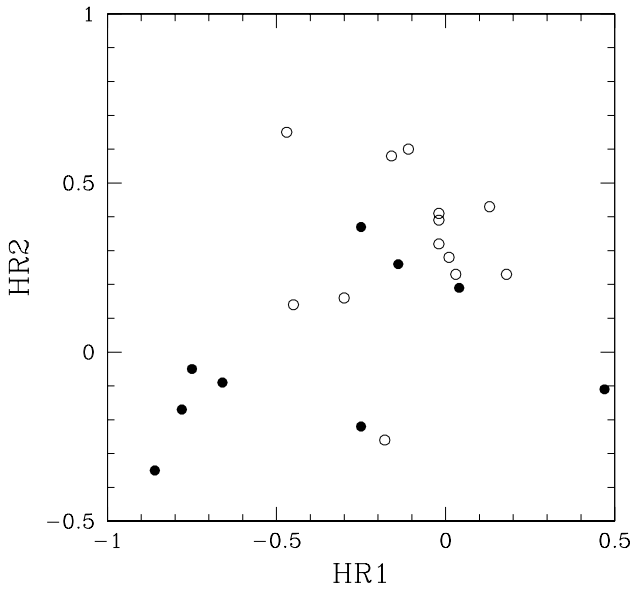

Fig. 9. Hardness ratio *HR*2 versus hardness ratio *HR*1 (see definition in Sect. 7.1). Each point represents an X-ray source for which both ratios are available. The filled points represent the sources which cross-correlate in position with an optical source.

have a positive value for HR_2, suggesting that most of them are obscured sources.

The line of sight towards WR 40 ($l_{\rm II}$ = 292.°31, $b_{\rm II}$ = –4.°83) is almost tangent to the Carina spiral arm. Therefore, one expects the neutral hydrogen column density along this direction to be quite large and to produce a substantial absorption of X-ray photons from extragalactic sources. In order to get a rough estimate of the total galactic extinction along this line of sight, we made use of the *DIRBE/IRAS* extinction maps provided by Schlegel et al. (1998). As pointed out by these authors, one has to be careful when using these maps near the galactic plane. In fact, for $|b_{\rm II}| \leq 5°$, some contaminating sources have not been removed from the maps and the temperature structure of the Galaxy is not well resolved at these low latitudes. Keeping these limitations in mind, we find that the *DIRBE/IRAS* maps indicate a relatively modest *E(B–V)* of 0.81 mag. Using the gas to dust ratio of Bohlin et al. (1978), we estimate a neutral hydrogen column density of $\sim 4.7\,10^{21}$ cm^{-2}. Assuming that extragalactic background sources have a power-law spectrum with a photon index of 1.4 and suffer a total interstellar absorption of $5\,10^{21}$ cm^{-2}, the detection limits $2\,10^{-3}$ and $1\,10^{-3}$ counts s^{-1} for the pn and MOS detectors translate into unabsorbed fluxes of $f_{\rm X}^{\rm unabs}(0.5-2.0\,{\rm keV}) = 3.8\text{–}5.7\,10^{-15}$ erg cm^{-2} s^{-1} and $f_{\rm X}^{\rm unabs}(2.0-10\,{\rm keV}) = 1.1\text{–}1.6\,10^{-14}$ erg cm^{-2} s^{-1}. Using the upper flux limits derived above in conjunction with the $\log N - \log S$ relation from Giacconi et al. (2001), we expect about 29 extragalactic sources in both energy bands. Although these calculations should be considered only as rough estimates (given the above-mentioned limitations), they indicate that a sizeable fraction of the serendipitous X-ray sources detected in the field around WR 40 might actually be associated with extragalactic objects. In fact, if we assume a total galactic column density twice as large as the value derived from the *DIRBE/IRAS* maps, we still end up with a substantial number of expected extragalactic sources (24 and 22 in the 0.5–2.0 keV and 2.0–10 keV bands respectively).

Only three sources are bright enough to allow the extraction of their X-ray spectra. For each of them, we generated the arf and rmf files with the corresponding SAS tasks.

7.3.1. Source #1

We used an ellipsoidal region to extract the spectrum of source #1. The region utilized to measure the background had the same shape but was positioned in the immediate vicinity while avoiding other sources. The spectrum was extracted for the three EPIC instruments. The spectrum of source #1 as seen with *XMM-Newton* peaks around 0.8–0.9 keV; no flux is visible above 5 keV. We used XSPEC (version 11.0.1) to fit the spectrum with various models. A simple one-temperature MEKAL model or even a two-temperature MEKAL model is not able to represent the data. A model that reasonably fits these data is an absorbed power-law with $N_{\rm H\,I} = 2.8\,10^{21}$ cm^{-2}, a photon index of 4.12 and a resulting $\chi^2_\nu = 0.98$ (with 82 degrees of freedom, dof = 82). A good fit is also obtained with a non-absorbed (result of the fit) three-temperature model, giving $kT_1 = 0.25$ keV, $kT_2 = 0.84$ keV and a less constrained $kT_3 = 3.39$ keV ($\chi^2_\nu = 0.93$, dof = 78). The best significant fit is an absorbed power-law plus MEKAL model, with $N_{\rm H\,I} = 0.66\,10^{21}$ cm^{-2}, a photon index of 2.86, a $kT = 0.77$ keV ($\chi^2_\nu = 0.89$, dof = 80). Typical relative errors on temperatures are about 20 per cent. If the X-ray source is identified with the F2V star HD 96309, the last two models are favoured because they propose a low absorption column that is more compatible with a rather nearby unreddened object. Indeed, the parallax of HD 96309 (see Perryman et al. 1997) indicates a distance of 124 pc quite compatible with the difference between the expected absolute magnitude of an F2V star (3.5 mag) and the apparent magnitude ($V = 8.91$) of the star, leaving little room for extinction. Depending on the model, the flux corrected for absorption is about $f_{\rm X}^{\rm unabs} = 7\,10^{-14}$ erg cm^{-2} s^{-1} corresponding, at the distance of HD 96309, to $L_{\rm X}(0.5-10\,{\rm keV}) = 1.3\,10^{29}$ erg s^{-1}.

Coronal X-ray emission from early-type F-type stars is frequently modelled by two temperature optically thin plasma models. Panzera et al. (1999) determined values of kT_1 and kT_2 in the ranges 0.06–0.2 keV and 0.3–0.7 keV. They further obtained X-ray luminosities from $L_{\rm X} \sim 10^{28}$ erg s^{-1} up to 10^{30} erg s^{-1}. While the luminosities are comparable to those of active G-K-M stars, the plasma temperatures of F-type stars are lower than in the later

spectral types. In this respect, we note that the best fit plasma temperatures of the EPIC spectra of source #1 are slightly, but not significantly, hotter than those of typical early F-type stars as quoted by Panzera et al. (1999). The X-ray luminosity appears quite compatible, leaving little doubt on the identification.

7.3.2. Source #6

Only the pn detector is usable for this source. The apparent X-ray spectrum peaks at 0.8 keV and at 0.5 keV. Very few counts are present above 3 keV. A good simple fit is given by a one-temperature MEKAL non-absorbed (result of the fit) model with $kT = 0.76$ keV ($\chi^2_\nu = 1.00$, dof = 62) or by a two-temperature MEKAL one with $N_{\rm H\,I} = 4.8\,10^{21}$ cm^{-2}, $kT_1 = 0.15$ keV, $kT_2 = 0.71$ keV ($\chi^2_\nu = 0.97$, dof = 60). The best fit is for an absorbed ($N_{\rm H\,I} = 1.7\,10^{21}$ cm^{-2}) MEKAL ($kT = 0.71$ keV) plus a power-law (photon index 3.98) model ($\chi^2_\nu = 0.91$, dof = 60). The solution with the largest column density is probably more compatible with the faintness of the possible optical counterpart.

7.3.3. Source #33

Finally, this source is only visible in the MOS2 because it is at the very edge of the field. The apparent spectrum peaks between 0.8 and 1.1 keV. A one-temperature model gives $N_{\rm H\,I} = 1.6\,10^{21}$ cm^{-2}, $kT = 0.58$ keV ($\chi^2_\nu = 0.88$, dof = 81). No improvement is possible by adding other MEKAL components; an extra power-law brings no real improvement either. The χ^2_ν is sufficiently good. The high extinction is rather compatible with the excess ($E(B-V) = 0.3$) of the source HD 96920 (G8III) but is anomalous when compared to its apparent brightness. From its parallax (see Perryman et al. 1997), indicating a distance of 250 pc, the star with $V = 7.2$ is too bright. The optical magnitude published by Eggen (1986) for HD 96920 is $V = 6.99$, confirming the problem.

The identification of sources #1 and #33, as well as some other cross correlations reported in Table 5 are indicative of the good quality of the astrometry.

8. Conclusions

In the present paper, we reported the analysis of an observation in the X-ray domain of the Wolf-Rayet star WR 40 and of its surrounding nebula RCW 58. This observation was obtained with the satellite *XMM-Newton* ($\sim$ 19 ks for each MOS detector, $\sim$ 12 ks for the pn). Neither the WR star WR 40 nor the nebula RCW 58 is detected. For the star, this lack of detection which we quantified ($L_{\rm X}/L_{\rm bol} \ll 2.6\,10^{-8}$) is in strong contrast with the marked photometric and spectroscopic variability of the star in the visible domain. Indeed, in ground based observations, the star exhibits a day-to-day, or even faster, variability, as well as indications of inhomogeneities in the wind. These characteristics could be related to the shocks and clumps that are intrinsic to radiatively driven strong winds and that are also expected to generate an X-ray emission. As a first step towards a possible interpretation, we estimated the opacity to X-rays of the ionized plasma constituting the wind. We showed that the optical depth of the wind of WR 40 is expected to be large enough to block, particularly in the range of energy typically below 2.5 keV, most of the photons that are emitted by any plasma buried in the wind deeper than about 20 R_*. Therefore, only hard X-ray emissions are expected. The X-ray emitting plasma must exist up to radii of 100 R_* to have a good chance of being observable outside the wind in the soft band and even in the medium band. Although little is known with certainty on the hydrodynamics of WR winds, it seems that their behaviour could be different in several aspects from the thin O-star winds (see Gayley & Owocki 1995). In any case, we expect that the majority of the shocks strong enough to produce X-rays occur rather deep into the wind. Therefore, it is perhaps not surprising that we did not detect WR 40 which has a rather dense and slow wind. If we join this result with the recent claim by Oskinova et al. (2003) that no single WC star has been up to now detected in the X-ray domain, we suggest that the X-ray emission from single normal WR stars could often be insignificant despite remarkable instabilities in the wind, just because of the large wind optical depth to X-rays. Further observations of WR stars are necessary to confirm this suggestion.

The non-detection of the nebula RCW 58 is also a puzzle. Indeed, most of the current studies and dedicated models of RCW 58 predict an X-ray luminosity larger than the very conservative upper limit we derived. Only the García-Segura and MacLow (1995) formalism tuned for RCW 58 and the model without mass loading by Arthur et al. (1996) give a value for the X-ray luminosity of the nebula that is of the same order of magnitude than our very conservative upper limit. A better knowledge of the actual X-ray background characteristics is expected to further tighten the constraints in the future, possibly up to a total rejection of the different existing models. We think that, compared to the WR bubbles NGC 6888 and S 308 which are detected in the X-ray domain, RCW 58 is much fainter due to a different status: RCW 58's morphology suggests that WR 40 could have gone through a Luminous-Blue-Variable ejection phase, while NGC 6888 and S 308 are suggested to have an RSG progenitor. However, the existence of such a phase for WR 40 has not yet been firmly demonstrated. In any case, the morphology of RCW 58 offers certainly a clue towards the explanation.

Finally, we detected 33 X-ray sources in the field, most of them being previously unknown. We established a catalog of these sources and performed the first steps towards their identifications.

Acknowledgements. The authors thank R. Ignace for a very careful reading of the manuscript. They are greatly indebted to the Belgian FNRS for multiple support. They also acknowledge financial support through PRODEX for the XMM-OM and INTEGRAL projects. Further support from the Belgian Federal Science Policy Office through contracts "Pôle

d'Attraction Interuniversitaire" P4/05 and P5/36 are also duly acknowledged. We further thank A. Detal, our system manager, for various helps to users, in particular concerning the SAS. This research has made use of the SIMBAD database, operated at CDS, Strasbourg, France.

References

Aldrovandi, S.M.V., & Péquignot, D., 1973, A&A, 25, 137
Antokhin, I.A., Bertrand, J.-F., Lamontagne, R., Moffat, A.F.J., & Matthews, J., 1995, AJ, 109, 817
Arnaud, M., & Rothenflug, R., 1985, A&AS, 60, 425
Arthur, S.J., Henney, W.J., & Dyson, J.E., 1996, A&A, 313, 897
Baade, D., & Lucy, L.B., 1987, A&A, 178, 213
Balona, L.A., Egan, J., & Marang, F., 1989, MNRAS, 240, 103
Berghöfer, T.W., Schmitt, J.H.M.M., Danner, R., & Cassinelli, J.P., 1997, A&A, 322, 167
Bohlin, R.C., Savage, B.D., & Drake, J.F., 1978, ApJ, 224, 132
Cassinelli, J.P., & Olson, G.L., 1979, ApJ, 229, 304
Cassinelli, J.P., Waldron, W.L., Sanders, W.T., et al., 1981, ApJ, 250, 677
Cassinelli, J.P., Miller, N.A., Waldron, W.L., MacFarlane, J.J., & Cohen, D.H., 2001, ApJ, 554, L55
Chen, W., & White, R.L., 1991, ApJ, 366, 512
Cherepashchuk, A.M., 1976, Sov. Astr. Letters, 2, 138
Cherepashchuk, A.M., & Aslanov, A.A., 1984, Ap&SS, 102, 97
Chu, Y.-H., 1988, PASP, 100, 986
Chu, Y.-H., Gruendl, R.A., & Guerrero, M.A., 2003a, Rev. Mex. Astron. Astrofis. Conf. Ser., 15, 62
Chu, Y.-H., Guerrero, M.A., Gruendl, R.A., García-Segura, G., & Wendker, H.J., 2003b, ApJ, 599, 1189
Cohen, D.H., de Messières, G.E., MacFarlane, J.J., et al., 2003, ApJ, 586, 495
De Becker, M., Rauw, G., Pittard, J.M., et al., 2004, A&A, 416, 221
Dessart, L., & Chesneau, O., 2002, A&A, 395, 209
Eggen, O.J., 1986, PASP, 98, 423
Feldmeier, A., Kudritzki, R.P., Palsa, R., Pauldrach, A.W.A., & Puls, J., 1997a, A&A, 320, 899
Feldmeier, A., Puls, J., & Pauldrach, A.W.A., 1997b, A&A, 322, 878
Feldmeier, A., Oskinova, L., & Hamann, W.R., 2003, A&A, 403, 217
Freyer, T., Hensler, G., & Yorke, H.W., 2003, ApJ, 594, 888
García-Segura, G., & Mac Low, M.M., 1995, ApJ, 455, 145
Gayley, K.G., & Owocki, S.P., 1995, ApJ, 446, 801
Giacconi, R., Rosati, P., Tozzi, P., et al., 2001, ApJ, 551, 624
Gosset, E., & Vreux, J.M., 1990, A&A, 231, 100
Gosset, E., Vreux, J.M., Manfroid, J., et al., 1989, MNRAS, 238, 97
Gosset, E., Rauw, G., Vreux, J.M., et al., 2003, in: K.A. van der Hucht, A. Herrero & C. Esteban, A Massive Star Odyssey, from Main Sequence to Supernova, Proc. IAU Symposium No. 212, (San Francisco: ASP), p.188
Grimm, H.J., Gilfanov, M., & Sunyaev, R., 2002, A&A, 391, 923
Gruendl, R.A., Chu, Y.-H., Dunne, B.C., & Points, S.D., 2000, AJ, 120, 2670
Gruendl, R.A., Guerrero, M.A., & Chu, Y.H., 2003, AAS meeting, 202, 32.16
Harnden, F.R.Jr., Branduardi, G., Elvis, M., et al., 1979, ApJ, 234, L51
Herald, J.E., Hillier, D.J., & Schulte-Ladbeck, R.E., 2001, ApJ, 548, 932
van den Heuvel, E.P.J., 1976, in: P. Eggleton, S. Mitton & J. Whelan, Structure and Evolution of Close Binary Systems, Proc. IAU Symposium No. 73, (Dordrecht: Reidel), p.35
Hillier, D.J., Kudritzki, R.P., Pauldrach, A.W.A., et al., 1993, A&A, 276, 117
Houk, N., & Cowley, A.P., 1975, *Catalogue of two dimensional spectral types for the HD stars, Vol. 1*, Michigan Spectral Survey, Ann Arbor, Dep. Astron., Univ. Michigan, 1
Ignace, R., Oskinova, L.M., & Brown, J.C., 2003, A&A, 408, 353
Jansen, F., Lumb, D., Altieri, B., et al., 2001, A&A, 365, L1
Jeffries, R.D., Thurston, M.R., & Pye, J.P., 1997, MNRAS, 287, 350
Kaastra, J.S., 1992, An X-ray spectral code for optically thin plasmas, Internal SRON-Leiden Report
Kaastra, J.S., & Mewe, R., 1993, A&AS, 97, 443
Kahn, S.M., Leutenegger, M.A., Cottam, J., et al., 2001, A&A, 365, L312
Katayama, H., Takahashi, I., Ikebe, Y., Matsushita, K., & Freyberg, M.J., 2004, A&A, 414, 767
Kramer, R.H., Cohen, D.H., & Owocki, S.P., 2003, ApJ, 592, 532
Krolik, J.H., & Kallman, T.R., 1984, ApJ, 286, 366
Lamers, H.J.G.L.M., & Morris, P.W., 1994, private communication
Lamontagne, R. & Moffat, A.F.J., 1987, AJ, 94, 1008
Lucy, L.B., 1982, ApJ, 255, 286
Lucy, L.B., & Solomon, P.M., 1970, ApJ, 159, 879
Lucy, L.B., & White, R.L., 1980, ApJ, 241, 300
Luo, D., McCray, R., & Mac Low, M.-M., 1990, ApJ, 362, 267
Marchenko, S.V., Moffat, A.F.J., Eversberg, T., et al., 1998, MNRAS, 294, 642
Marston, A.P., Yocum, D.R., García-Segura, G., & Chu, Y.-H., 1994, ApJS, 95, 151
Matthews, J.M. & Moffat, A.F.J., 1994, A&A, 283, 493
Mewe, R., Gronenschild, E.H.B.M., & van den Oord, G.H.J., 1985, A&AS, 62, 197
Mewe, R., Raassen, A.J.J., Cassinelli, J.P., et al., 2003, A&A, 398, 203
Miller, N.A., Cassinelli, J.P., Waldron, W.L., MacFarlane, J.J., & Cohen, D.H., 2002, ApJ, 577, 951
Moffat, A.F.J., & Isserstedt, J., 1980, A&A, 91, 147
Oskinova, L.M., Ignace, R., Hamann, W.-R., Pollock, A.M.T., & Brown, J.C., 2003, A&A, 402, 755
Owocki, S.P., Castor, J.I., & Rybicki, G.B., 1988, ApJ, 335, 914
Panzera, M.R., Tagliaferri, G., Pasinetti, L., & Antonello, E., 1999, A&A, 348, 161
Perryman, M.A.C., Lindegren, L., Kovalevsky, J., et al. , 1997, A&A, 323, L49
Pittard, J.M., & Stevens, I.R., 1997, MNRAS, 292, 298
Pittard, J.M., & Stevens, I.R., 2002, A&A, 388, L20
Pollock, A.M.T., 1987, ApJ, 320, 283
Pollock, A.M.T., Haberl, F., & Corcoran, M.F., 1995, in: eds. K.A. van der Hucht & P.M. Williams, Wolf-Rayet stars: binaries, colliding winds, evolution, proceedings of IAU Symp. No.163, (Dordrecht: Kluwer Academic Publ.), p.512
Prilutskii, O.F., & Usov, V.V., 1976, Sov. Astr., 20, 2
Raassen, A.J.J., van der Hucht, K.A., Mewe, R., et al., 2003, A&A, 402, 653

Rauw, G., 1997, PhD thesis, Contribution à l'étude de systèmes binaires massifs: détermination des paramètres fondamentaux et analyse des processus d'interaction dans des systèmes de type Of et WNL, Université de Liège.
Rauw, G., Vreux, J.M., Gosset, E., et al., 1996, A&A, 306, 771
Rauw, G., Blomme, R., Waldron, W.L., et al., 2002, A&A, 394, 993
Runacres, M.C., & Owocki, S.P., 2002, A&A, 381, 1015
Sasaki, M., Pietsch, W., & Haberl, F., 2003, A&A, 403, 901
Schlegel, D.J., Finkbeiner, D.P., & Davis, M., 1998, ApJ, 500, 525
Seward, F.D., & Chlebowski, T., 1982, ApJ, 256, 530
Seward, F.D., Forman, W.R., Giacconi, R., et al., 1979, ApJ, 234, L55
Shull, J.M., & van Steenberg, M., 1982, ApJS, 48, 95 (errata: 49, 351)
Skinner, S.L., Güdel, M., Schmutz, W., & Stevens, I.R., 2001, ApJ, 558, L113
Skinner, S.L., Zhekov, S.A., Güdel, M., & Schmutz, W., 2002a, ApJ, 572, 477
Skinner, S.L., Zhekov, S.A., Güdel, M., & Schmutz, W., 2002b, ApJ, 579, 764
Smith, L.F., & Batchelor, R.A., 1970, Austr. Journal of Physics, 23, 203
Smith, L.J., 1996, in: eds. J.-M. Vreux, A. Detal, D. Fraipont-Caro, E. Gosset, & G. Rauw, Wolf-Rayet stars in the Framework of Stellar Evolution, proceedings of the 33rd Liège International Colloquium, Liège University, p.381
Smith, L.J., Pettini, M., Dyson, J.E., & Hartquist, T.W., 1984, MNRAS, 211, 679
Smith, L.J., Lloyd, C., & Walker, E.N., 1985, A&A, 146, 307
Smith, L.J., Pettini, M., Dyson, J.E., & Hartquist, T.W., 1988, MNRAS, 234, 625
Stella, L., White, N.E., & Rosner, R., 1986, ApJ, 308, 669
Stevens, I.R., Blondin, J.M., & Pollock, A.M.T., 1992, ApJ, 386, 265
Strüder, L., Briel, U., Dennerl, K., et al., 2001, A&A, 365, L18
Turner, M.J.L., Abbey, A., Arnaud, M., et al., 2001, A&A, 365, L27
Tutukov, A.V., & Cherepashchuk, A.M., 2003, Astr. Reports, 47, 386
Verner, D.A., & Ferland, G.J., 1996, ApJS, 103, 467
Verner, D.A., & Yakovlev, D.G. 1995, A&AS, 109, 125
Verner, D.A., Ferland, G.J., Korista, K.T., & Yakovlev, D.G., 1996, ApJ, 465, 487
Voronov, G.S., 1997, Atomic Data and Nuclear Data Tables, 65, 1
Waldron, W.L., 1984, ApJ, 282, 256
Waldron, W.L., & Cassinelli, J.P., 2000, ApJ, 548, L45
Weaver, R., McCray, R., Castor, J., Shapiro, P., & Moore, R., 1977, ApJ, 218, 377 (errata: 220, 742)
Wessolowski, U., 1996, MPE report, 263, 75
Woods, D.T., Shull, J.M., & Sarazin, C.L., 1981, ApJ, 249, 399
Wrigge, M., Wendker, H.J., & Wisotzki, L., 1994, A&A, 286, 219

List of Objects